Contents lists available at ScienceDirect

Bioactive Materials

Fabricating oxygen self-supplying 3D printed bioactive hydrogel scaffold for augmented vascularized bone regeneration

Yang Yang [a], Wanmeng Wang [b], Qianrui Zeng [a], Ning Wang [b], Wenbo Li [a], Bo Chen [b], Qingxin Guan [a,*], Changyi Li [b,***], Wei Li [a,**]

[a] *State Key Laboratory of Elemento-Organic Chemistry, Key Laboratory of Advanced Energy Materials Chemistry (Ministry of Education), College of Chemistry, Nankai University, Tianjin, 300071, PR China*
[b] *Tianjin Key Laboratory of Oral Soft and Hard Tissues Restoration and Regeneration, School of Stomatology, Tianjin Medical University, Tianjin, 300071, PR China*

ARTICLE INFO

ABSTRACT

Limited cells and factors, inadequate mechanical properties, and necrosis of defects center have hindered the wide clinical application of bone-tissue engineering scaffolds. Herein, we construct a self-oxygenated 3D printed bioactive hydrogel scaffold by integrating oxygen-generating nanoparticles and hybrid double network hydrogel structure. The hydrogel scaffold possesses the characteristics of extracellular matrix; Meanwhile, the fabricated hybrid double network structure by polyacrylamide and $CaCl_2$-crosslinked sodium carboxymethylcellulose endows the hydrogel favorable compressive strength and 3D printability. Furthermore, the O_2 generated by CaO_2 nanoparticles encapsulated in ZIF-8 releases steadily and sustainably because of the well-developed microporous structure of ZIF-8, which can significantly promote cell viability and proliferation *in vitro*, as well as angiogenesis and osteogenic differentiation with the assistance of Zn^{2+}. More significantly, the synergy of O_2 and 3D printed pore structure can prevent necrosis of defects center and facilitate cell infiltration by providing cells the nutrients and space they need, which can further induce vascular network ingrowth and accelerate bone regeneration in all areas of the defect *in vivo*. Overall, this work provides a new avenue for preparing cell/factor-free bone-tissue engineered scaffolds that possess great potential for tissue regeneration and clinical alternative.

1. Introduction

Regeneration of large bone defects that occurred in trauma and disease has always been challenging [1]. As autologous and allograft bone grafts suffer from the significant complications, limited availability, and age restrictions, developing advanced bone-tissue engineering scaffolds is of great importance [2]. It is well-acknowledged that bone is a highly vascularized tissue that develops after angiogenesis [3]. Many studies have demonstrated that delivery of cells such as stem cells or growth factors can effectively stimulate angiogenesis and osteogenesis, while short half-time, high cost, and limited resources restrict their widespread application [4]. Consequently, a cell/factor-free scaffold that can provide a favorable microenvironment to significantly promote vascularized bone regeneration needs to be explored for further clinical treatment.

Recently, O_2 has received much attention in tissue engineering owing to the important role in cellular metabolism [5]. Given that the effective diffusion distance of O_2 in vasculature is 100–200 μm, cell death and tissue necrosis might occur at the bone defects center due to the destruction and untimely reconstruction of vascular network [6]. It has been reported that timely and adequate O_2 supply before angiogenesis are critical for preventing tissue necrosis and improving cellular survival, while promoting tissue repair by enhancing vascular-related genes expression and differentiation of osteoblasts [7,8]. Typically, O_2 releasing materials are divided into oxygen-carrying and oxygen-generating materials [9]. Oxygen-carrying materials such as natural haemoglobin, perfluorocarbons and cyclodextrin are possible to cause cell damage due to the burst release of O_2 within a few hours [10, 11]. In addition, the release time of O_2 is too short to support reconstruction of the vascular network for 2–4 weeks [12]. To meet the time

requirements, oxygen-generating materials such as CaO_2, ZnO_2, and MgO_2 were proposed, which could deliver O_2 for up to one week by attaching to scaffolds or embedding into hydrogels [13,14]. With further improvements, the O_2 generation time has been doubled by encapsulating CaO_2 in polycaprolactone (PCL) microspheres [15,16]. However, the compressive modulus of the resulting scaffold is around 20 KPa due to the large size of polymer microspheres embedded in the hydrogel scaffolds, which is seemingly insufficient to support the bone defects. In addition to polymer microspheres, metal-organic frameworks (MOFs) have been widely used to serve as unique host matrices for various small molecule drugs because of the well-developed pore structure and large surface areas [17]. Furthermore, the 3D structure of MOFs offers the opportunity to develop new types of composite materials by encapsulating functional nanoparticles in cavities [18]. Compared with polymer microspheres without pores, MOFs-encapsulated solid peroxides can provide continuous O_2 through well-develop micropores, and the size of the composite nanoparticles is smaller. Therefore, exploiting novel oxygen-generating nanoparticles by MOFs encapsulation has great potential to achieve a stable and sustained O_2 release without affecting the mechanical properties of the scaffolds.

Besides the beneficial effects of O_2, a suitable pore size of scaffold also displays the remarkable capacity of constructing a favorable microenvironment for angiogenesis and bone regeneration. Studies have found that the porous structure around 10 μm can facilitate efficient exchange of mineral ions and introduction of bone-forming proteins. However, this size limits cell infiltration into the scaffold, which might result in inefficient repair of the defects center and even tissue necrosis [19]. To mitigate these limitations, pore sizes ranging from 300 to 800 μm have been investigated, which exhibited the ability to effectively induce blood vessels and bones ingrowth by allowing cells to infiltrate and shuttle [20,21]. To integrate the multi-level pore size structure, the manufacturing method of 3D printing has great advantage due to its architecture customization and high precision. In comparison with solid 3D printing bioinks such as calcium phosphate, hydroxyapatite, and poly(ε-caprolactone), hydrogels have attracted much attention due to the similar properties to extracellular matrices, porous internal structure, and good toughness [22–25]. Moreover, the ability of hydrogels to encapsulate drugs enables their integration with nanoparticles or cells for multi-functionality [26,27]. However, the weak mechanical strength of bioactive hydrogels limits their extensive application in bone tissue engineering [28,29]. Most hydrogels used for 3D printing bioinks are composed of single network, making their compressive strength essentially less than 1.0 MPa [30–32]. Many efforts have been made to explore hybrid double network hydrogel structure that possesses both stiffness and toughness, while its integration with 3D printing requires consideration of many factors such as curing speed, curing method, and precursor viscosity [33,34]. The combination of acrylamide and sodium alginate have been used of 3D printing bioink, which can form hybrid double network hydrogel structure [35]. However, since sodium alginate solidifies rapidly when exposed to Ca^{2+} during bioink preparation, the viscosity of the solution is difficult to control and the mechanical strength of the final hydrogel may be compromised [36,37]. Sodium carboxymethylcellulose can also be cross-linked by Ca^{2+} to form physical network that is still viscous liquid [38]. Therefore, it is more suitable for combination with acrylamide for 3D printing, which is possible to achieve excellent mechanical strength at the same time. Accordingly, by designing and constructing a hybrid double network hydrogel structure composed of acrylamide and sodium carboxymethylcellulose that can be 3D printed, both excellent mechanical properties and multi-level pore size structure can be achieved. Moreover, the hydrogel can integrate with oxygen-generating nanoparticles, which might further enhance the mechanical strength and achieve multi-functionality.

Herein, a Gel/ZIF-8-CaO_2 bioactive hydrogel scaffold combining oxygen-generating nanoparticles with hybrid double network hydrogel has been successfully constructed by MOFs encapsulation and 3D printing. It can achieve long-term O_2 self-supplying, multi-level pore size structure, and excellent mechanical properties to significantly enhance vascularized bone regeneration without the addition of cells or factors (Scheme 1). First, the polyvinyl pyrrolidone (PVP)-modified CaO_2 nanoparticles (CaO_2-PVP) with particle sizes below 20 nm were prepared. Then, ZIF-8 was utilized to encapsulate CaO_2-PVP in cavities (ZIF-8-CaO_2) through weak coordination interactions and hydrophobic interactions between PVP and ZIF-8. Subsequently, the Gel/ZIF-8-CaO_2 composite scaffold was fabricated by 3D printing the bioink consisting of acrylamide, $CaCl_2$-crosslinked sodium carboxymethylcellulose and ZIF-8-CaO_2 nanoparticles. *In vitro* experiments demonstrated that the sustained release of O_2 could apparently promote cell proliferation and differentiation, and initiate timely angiogenesis and osteogenesis. *In vivo* subcutaneous model and cranial bone defect model of rats confirmed that the synergy of O_2 and 3D printed pore structure could promote simultaneous bone regeneration of the defect edge and center by providing a favorable microenvironment for cell infiltration, vascular network reconstruction, and bone formation. Taken together, this work provides an effective strategy for the fabrication of cell/factor-free bone-tissue engineering scaffolds with great potential for clinical application.

2. Materials and methods

2.1. Synthesis of CaO_2-PVP and bulk CaO_2

In a typical synthesis, $CaCl_2 \cdot 2H_2O$ (0.6 g) and PVP (0.6 g) were dissolved in 30 mL anhydrous methanol with the help of stirring. Subsequently, the mix solution of 480 μL H_2O_2 and 1 mL ammonia solution was added. The mix solution reacted under stirring for 1 h at 0 °C. The as-obtained precipitate was collected by centrifugation, followed by washing with methanol for three times and dispersing in 1 mL methanol for later use. The obtained sample was named as CaO_2-PVP. The synthesis process of bulk CaO_2 was the same except for PVP doping. The obtained sample was named as CaO_2.

### 2.2. Synthesis of ZIF-8-CaO_2, ZIF-8, and ZIF-8/CaO_2

$Zn(NO_3)_2 \cdot 6H_2O$ (37.2 mg, 0.13 mmol) was dissolved in 4 mL methanol after adding 1 mL CaO_2-PVP dispersion, which was then added to 5 mL of methanol containing 2-methylimidazole (10.3 mg, 0.13 mmol). The mixed solution was kept for 24 h at room temperature. The resulting precipitate was centrifuged, washed three times in methanol, and dried overnight at 60 °C under vacuum. The obtained sample was named as ZIF-8-CaO_2. Pure ZIF-8 was synthesized under the same condition without CaO_2 doping. For the preparation of ZIF-8/CaO_2, the synthesized ZIF-8 and 1 mL CaO_2-PVP dispersion were added to 9 mL methanol, and the further treatment was the same as for ZIF-8-CaO_2.

2.3. Synthesis of 3D printed Gel, Gel/ZIF-8, Gel/ZIF-8-CaO_2 scaffolds

Taking the Gel/ZIF-8-CaO_2 as an example, acrylamide (2.34 g), ZIF-8-CaO_2 (0.15 g), sodium carboxymethylcellulose (0.8 g), $CaCl_2$ (0.65 g), Bis (0.05 g), and V50 (0.09 g) were added to 10 mL deionized water under stirring to form a homogeneous suspension (The mass ratio of CC to $CaCl_2$ is 1.23). Gel/ZIF-8 bioink was synthesized by replacing ZIF-8-CaO_2 with ZIF-8.

The synthesis of the Gel bioink was the same without the addition of ZIF-8 or ZIF-8-CaO_2 nanoparticles. By keeping the mass of $CaCl_2$ in 10 mL deionized water constant, we prepared Gel bioinks of different viscosities by adjusting the amount of CC (The mass ratio of CC and $CaCl_2$ is 1.00, 1.23 and 1.46, respectively).

The bioink was loaded into a sample tube for further 3D printing. We designed the 3D printed scaffold structure (3 mm × 3 mm × 0.8 mm) with Blender and Cura software and loaded them into printer. The other models were downloaded from the LuckyBot ONE website. The printing process was performed at room temperature using a 0.30 mm diameter (inner diameter) stainless steel extrusion needle. The scaffolds were
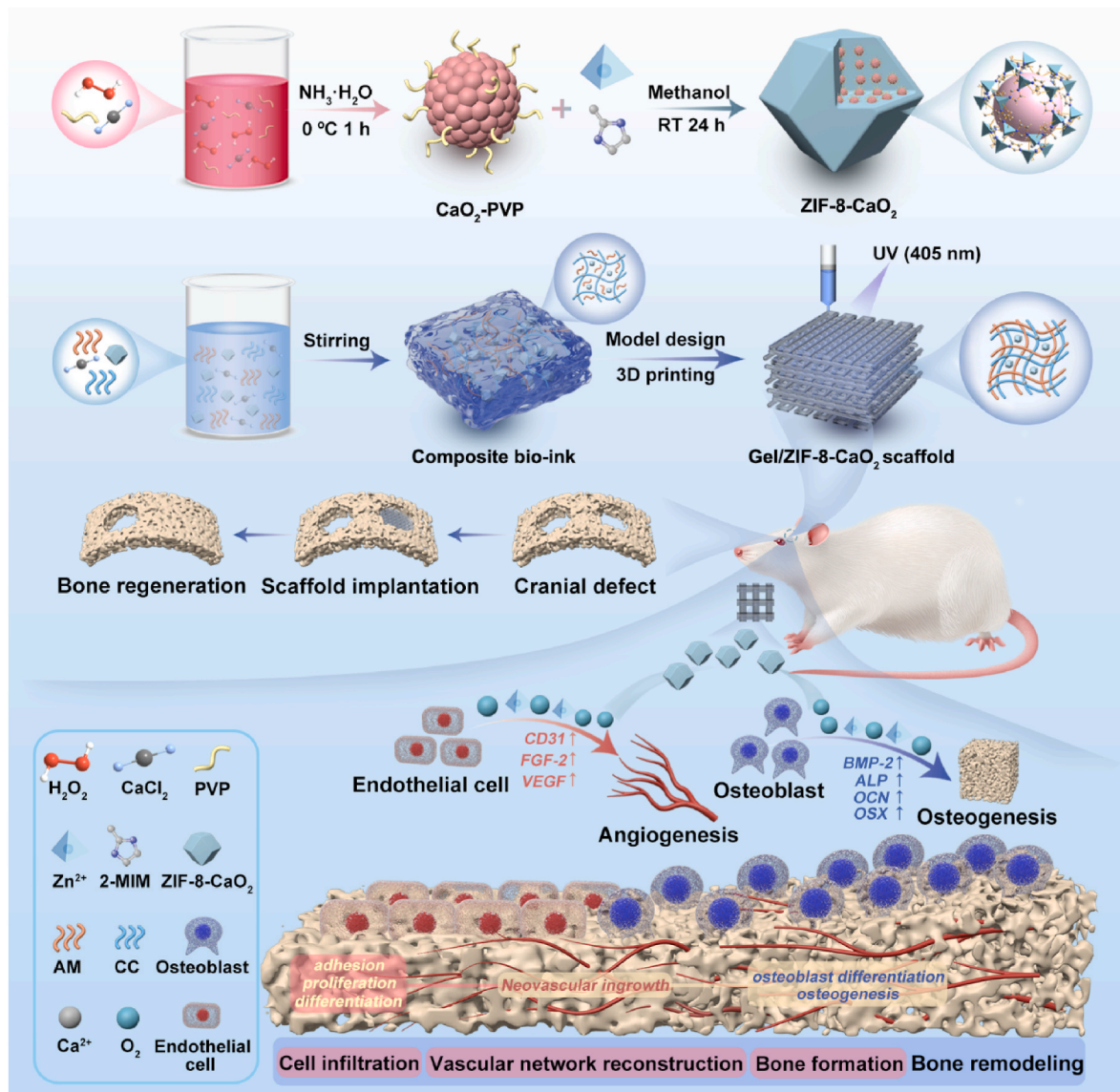
Scheme 1. Schematic illustration for the preparation of 3D printed Gel/ZIF-8-CaO$_2$ composite scaffold and the significant effect in augmented vascularized bone regeneration.

printed layer-by-layer with a starting angle of 0° and a rotation angle of 90°. The moving speed of extrusion needle was 50 mm s^{-1} and the extrusion speed was 4 mm s^{-1}. The printing process was performed under 405 nm UV light. Acrylamide was rapidly cross-linked under UV light during printing, which allowed the hydrogel to be cured immediately. After printing, the front and back of the printed scaffolds were irradiated for 10 min each to ensure complete curing and homogeneity.

2.4. Cell culture

MC3T3-E1 cells (ATCC, CRL-2594) and HUVECs (ATCC, PCS-100-010) were obtained from ATCC Cell Bank (Manassas, VA, USA). MC3T3-E1 cells and HUVECs were cultured in DMEM medium with the supplement of 10 % FBS and 1 % PS at 37 °C under 5 % CO$_2$.

2.5. Cytocompatibility evaluation of scaffolds

For the Gel, Gel/ZIF-8, and Gel/ZIF-8-CaO$_2$ scaffolds, MC3T3-E1 cells were seeded at a density of 1×10^4 cell/well on the scaffolds surface in 24-well plates and the medium was changed every two days.

For cell adhesion and morphological observation, cells were cultured for 1, 4, and 7 days and then fixed with 4 % paraformaldehyde for 30 min at room temperature. Phalloidin-Rhodamine and DAPI were used to stain the cytoskeleton and nucleus, respectively. For the further cell adhesion observation, cells were cultured for 2 days and then fixed with 4 % paraformaldehyde for 30 min at room temperature. Vinculin, Phalloidin-Rhodamine, and DAPI were used to stain the focal adhesion protein, cytoskeleton, and nucleus. Confocal laser scanning microscopy (CLSM, FV3000RS, Olympus, Japan) was used to acquire fluorescent stained images.

For cell proliferation evaluation, CCK-8 and living/dead cell assays were implemented on 1, 4, and 7 days, respectively. For CCK-8 assay, 300 μL culture medium and 10 % CCK-8 working solution were added to each well and incubated at 37 °C for 1 h. Then, 100 μL of the supernatant was added to a 96-well plate. The absorbance at 450 nm was detected using a microplate reader (VARIOSKAN FLASH, Thermo, USA). For living/dead cell assay, the cells were gently washed with PBS twice at each time point and then stained with a live/dead staining kit followed the manufacturer's protocol. The stained cells were imaged by an invert fluorescence microscope (TH4-200, Olympus, Japan).

2.6. HUVECs migration assay

HUVECs were seeded at a density of 6×10^4 cell/well into 24-well plates for about 24 h until approximately 80 % confluence. Scratches were made with a 200 μm pipette tip in the middle of the well, and the medium was replaced with the scaffolds extract (with 1 % FBS). The scratches were photographed with an inverted microscope (IX71, Olympus, Japan) at 0 and 24 h, respectively, and quantified by ImageJ software.

2.7. HUVECs tube formation assay

100 μL Matrigel was transferred into 48-well culture plates and incubated at 37 °C for 1 h. HUVECs were seeded on the Matrigel surface at a density of 3×10^4 cell/well. The cells were incubated with extracts (with 1 % FBS) at 37 °C for 8 h and photographed using an inverted microscope (IX71, Olympus, Japan). The tubular-network formation parameters were quantified by ImageJ software.

2.8. Osteogenic and angiogenic genes expression

MC3T3-E1 cells were seeded at a density of 1×10^4 cell/well into 24-well plates, and incubated with extracts at 37 °C for 7 and 14 days. The total RNAs of the cells were extracted with TRIzol reagent and reverse transcribed to produce complementary DNA (cDNA). The qRT-PCR was carried out to evaluate the relative RNA expression level using the housekeeping gene glyceraldehyde-3-phosphate dehydrogenase (*GAPDH*) as a loading control. The amplification reaction was performed with SYBR Green detection reagent (Yeason, 11201ES03, Shanghai, P. R. China) for 40 cycles, and the relative expression of target genes was calculated by the $2^{-\Delta\Delta Ct}$ method. HUVECs were seeded at a density of 1×10^4 cell/well into 24-well plates, and incubated with extracts at 37 °C for 3 and 7 days. The subsequent operation was the same as the procedure of MC3T3-E1 cells. The primer sequences used to measure the expression of osteogenesis and angiogenesis related genes are shown in Table S3 and Table S4.

2.9. Alkaline phosphatase staining

MC3T3-E1 cells were seeded at a density of 2×10^4 cell/well into 24-well plates, and incubated at 37 °C until approximately 90 % confluence. The cells were cultured in osteoconductive media (containing 10 mM β-glycerophosphate, 50 μg/mL ascorbic acid, and 10^{-4} mM dexamethasone) added with the scaffolds extract for 7 days at 37 °C. At the scheduled time, the cells were fixed with 4 % paraformaldehyde for 30 min. The cells were washed with deionized water and incubated with the BCIP/NBT kit. The cells were washed with deionized water and the images were obtained with camera and inverted microscope (IX71, Olympus, Japan).

2.10. Alizarin Red S staining and quantitative analysis

MC3T3-E1 cells were seeded at a density of 2×10^4 cell/well into 24-well plates, and incubated at 37 °C until approximately 90 % confluence. The cells were cultured in osteoconductive media added with the scaffolds extract for 14 days at 37 °C. At the scheduled time, the cells were fixed with 4 % paraformaldehyde for 30 min at room temperature. The cells were washed with deionized water and incubated with the Alizarin Red S Staining Kit for Osteogenesis (pH = 4.2). The cells were washed with deionized water and the images were obtained with camera and inverted microscope (IX71, Olympus, Japan). For quantitation, acetic acid was added to each well and incubated overnight at room temperature. The collected supernatants were neutralized with ammonia and the OD values were read at 405 nm.

2.11. Subcutaneous implantation in rats

All animal experiments were approved by the Animal Care and Welfare Committee of Tianjin Nankai Hospital (Approval No. NKYY-DWLL-2023-066), and performed in compliance with the Guidelines for Care and Use of Laboratory Animals. The SD rats (8 weeks old, 250 g, male) were provided by the experimental center of Tianjin Nankai Hospital and randomly divided into five groups. The rats were anesthetized by intraperitoneal injection of pentobarbital sodium with 2 %. Two longitudinal incisions of approximately 1 cm were made on both sides of the dorsal skin of each rat to form a subcutaneous pocket and placed into sterile scaffolds. After surgery, the rats were housed and allowed to eat and drink. Two weeks after implantation, samples were harvested and fixed in 4 % paraformaldehyde. The samples were then processed for hematoxylin and eosin (H&E) staining and immunofluorescence staining. Images were obtained by positive fluorescence microscope (NE910, Nexcope, America) and CLSM, respectively. The immunofluorescence staining was quantified by ImageJ software.

2.12. Bone defect reconstruction in rats

The skull defect model was used to evaluate the effect of different scaffolds on bone regeneration. The rats were randomly divided into four groups for further experiments. After anesthesia with 2 % sodium pentobarbital, two circular defects with a diameter of 5 mm were created on both sides of the rat skull and then imbedded with scaffolds. After 4 and 12 weeks of implantation, the samples were collected and fixed in 4 % paraformaldehyde. The samples were scanned and reconstructed by micro-CT. The bone tissue volume/total tissue volume (BV/TV) value and trabecular number (Tb.N) value of the region of interest were calculated by CT-Analyzer software. Besides, major organs (heart, liver, spleen, lung, and kidney) were collected after 12 weeks of implantation to evaluate biosafety of different scaffolds *in vivo*.

2.13. Histological analysis

The samples of skull defects were decalcified in EDTA solution and embedded in paraffin. Subsequently, the samples were cut into 5 μm sections and processed for hematoxylin and eosin (H&E) and Masson's trichrome staining. The immunofluorescence staining of CD31 and α-SMA was performed at 4 weeks to assess the angiogenesis of skull defects, and the OCN staining was carried out at 12 weeks to assess the osteogenesis. The samples of major organs were processed for H&E staining with a 5 μm section. Images were obtained by positive fluorescence microscope and CLSM and quantified by ImageJ software.

2.14. RNA sequencing and data analysis

MC3T3-E1 cells were seeded at a density of 1×10^4 cell/well into 24-well plates, and incubated with extracts at 37 °C for 7 days. The total RNAs of the cells were extracted with TRIzol reagent and stored at -80 °C before sequencing. The purity and concentration were measured by NanoDrop 2000 (Invitrogen, USA). RNA sequencing was performed by Illumina HiSeq X10 (Illumina, USA) and the results were analyzed by free online novomagic Clound Platform (https://magic.novogene.com/). Differentially expressed genes (DEGs) were selected with |fold-change| > 1.5 and *p-value* < 0.05. GSEA was analyzed with |NES| > 1, Nominal *p-value* < 0.05 and FDR <0.25.

2.15. Statistical analysis

All data were expressed as mean ± standard deviation (SD). All statistical analyses were performed by one-way analysis of variance (ANOVA). Significant differences were considered when *p < 0.05, **p < 0.01, and ***p < 0.001.*

3. Results and discussion

3.1. Preparation and characterization of ZIF-8-CaO₂ nanoparticles

To achieve steady and sustainable oxygen-generating, porous MOFs were utilized as hosts to in-situ trap CaO_2 guests in their cages during MOFs crystallization. ZIF-8 was chosen as the encapsulated hosts because of the effect of Zn^{2+} in promoting angiogenesis and bone regeneration, as well as its strong coordination ability [39,40]. PVP was introduced to prevent CaO_2 from aggregating into clumps by forming coordination with Ca^{2+} and simultaneously enhanced CaO_2 affinity to ZIF-8 through the weak coordination interaction between the pyrrolidone rings of PVP (C=O) and Zn^{2+} in ZIF-8 [41].

The powder X-ray diffraction (XRD) patterns show that no peaks of CaO_2-PVP were detected in comparison with the obvious typical peaks of bulk CaO_2, which was probably due to its small size (Fig. 1A). Scanning electron microscope (SEM) and transmission electron microscope (TEM) images reveal that stable and well-dispersed spherical polycrystalline CaO_2-PVP with uniform size around 18 nm were prepared thanks to the protective layer formed by the adsorbed PVP on the nanoparticles surface (Fig. 1D and E). However, the CaO_2 obtained by direct mixing of $CaCl_2$, H_2O_2, and $NH_3 \cdot H_2O$ in methanol appeared to be bulk due to heavy agglomeration (Fig. S1, Supporting Information), demonstrating the ability of PVP to stabilize CaO_2 in small particles, which was consistent with the results of SEM and TEM. Uniform particle sizes around 18 nm and the absence of other impurity peaks in XRD pattern can basically ensure the success of synthesis and the purity of the

product. In addition, the successful synthesis of bulk CaO_2 have been confirmed by XRD pattern, and the addition of PVP under the same synthetic conditions will not change the final product in previous study [42]. To further prove the successful synthesis and the purity of CaO_2-PVP, XRF and XPS were applied to illustrate the existing elements. The XRF results showed the presence of only Ca in bulk CaO_2 and CaO_2-PVP, indicating that $CaCl_2$ had reacted with no residue (Table S1, Supporting Information). The XPS results showed that only Ca and O elements could been obviously detected in the bulk CaO_2 and CaO_2-PVP at an atomic ratio around 1:2 (Fig. S2, Supporting Information) [14]. The elements in PVP were not significantly detected, probably due to the lower content compared to CaO_2. Moreover, we conducted a test on the ability of CaO_2-PVP to release oxygen (Fig. S3, Supporting Information). We dispersed the well-washed CaO_2-PVP in 5 mL of deionized water for testing, while preparing 5 mL deionized water containing 480 μL H_2O_2 to exclude the effect of O_2 release from the residual H_2O_2 and 5 mL pure deionized water as control. 150 μL HNO_3 solution (5 M) was added to each prepared sample to produce an obvious O_2 release. The CaO_2-PVP group exhibited an obvious O_2 release as the turbid liquid became clear compared with the H_2O_2 group and pure deionized water group. As a result, the above results demonstrated that the CaO_2-PVP nanoparticles were successfully synthesized and no other particles or reactants were obviously introduced.

The methanolic solution of CaO_2-PVP was then briefly mixed with zinc nitrate and 2-methylimidazole, followed by standing for 24 h. The XRD patterns show that the crystalline texture of ZIF-8-CaO₂ was unaffected by the introduction of CaO_2, and the broad peak at 25° of ZIF-8-
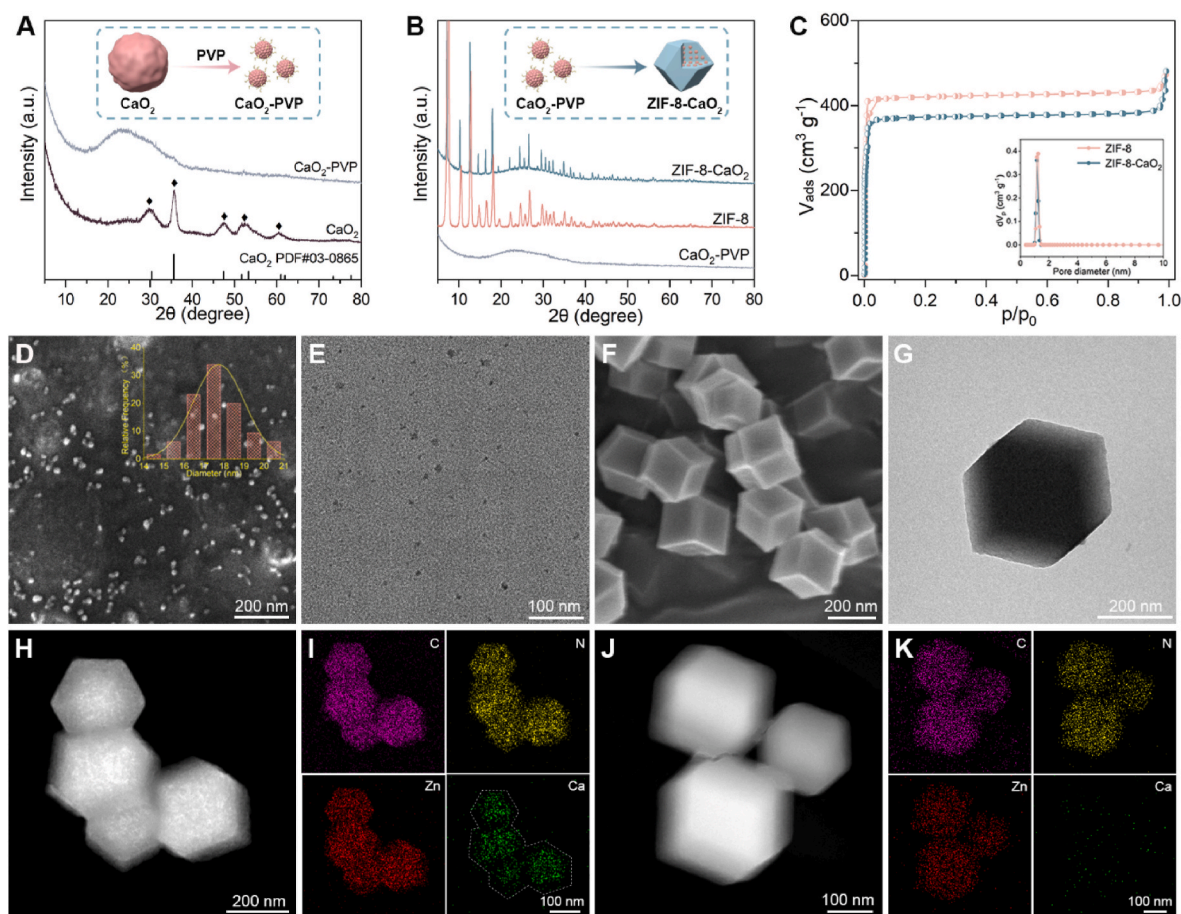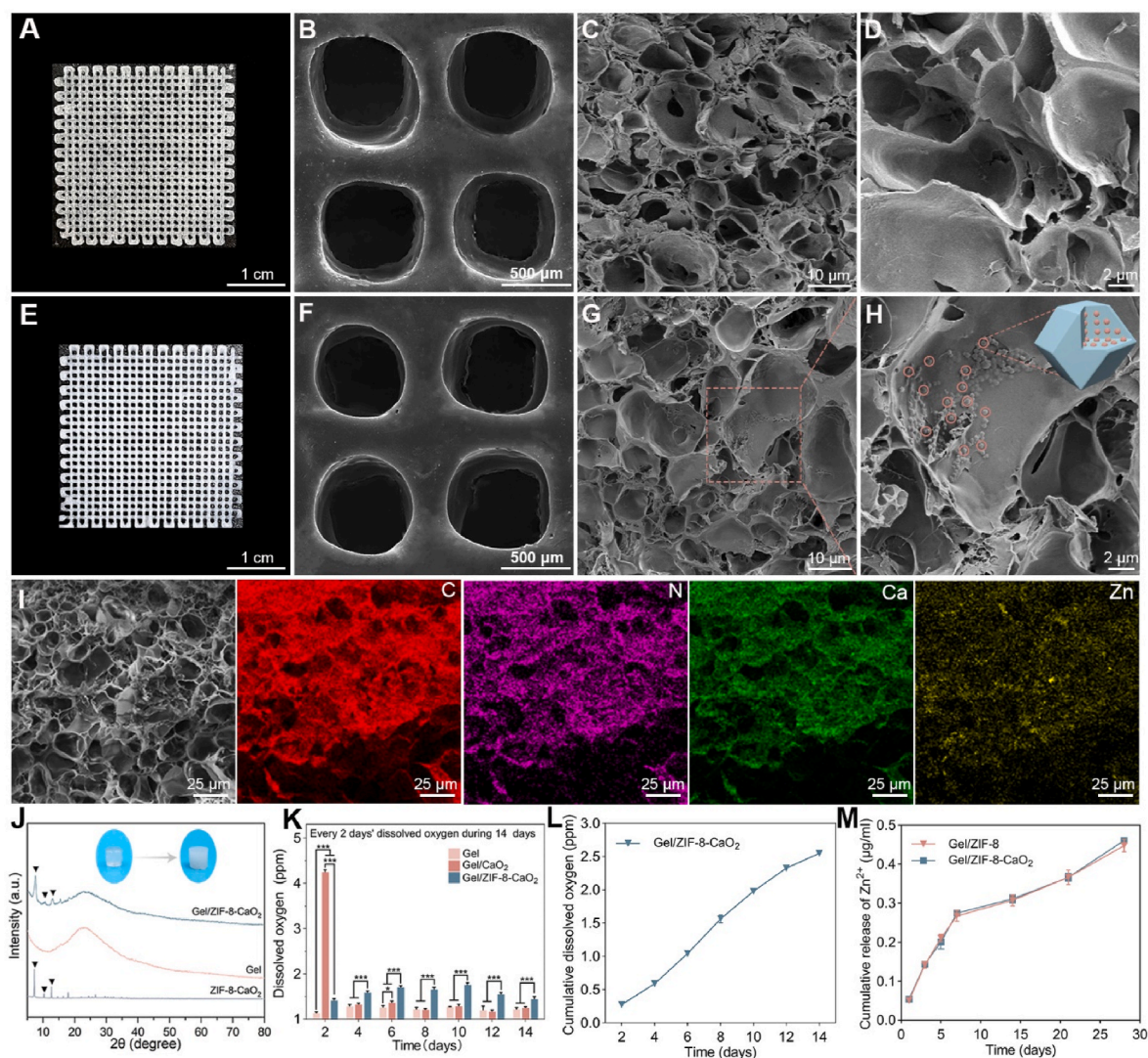

Fig. 1. Physical characterizations of CaO₂-PVP and ZIF-8-CaO₂. A) XRD patterns of CaO₂ and CaO₂-PVP. B) XRD patterns of CaO₂-PVP, ZIF-8, and ZIF-8-CaO₂. C) Nitrogen sorption isotherms of ZIF-8 and ZIF-8-CaO₂ (inset shows the pore size distribution). D) SEM image of CaO₂-PVP (inset shows the histogram of size distribution). E) TEM image of CaO₂-PVP. F) SEM image and G) TEM image of ZIF-8-CaO₂. H) TEM image and I) corresponding EDS elemental mapping results of ZIF-8-CaO₂. J) TEM image and K) corresponding EDS elemental mapping results of ZIF-8/CaO₂.

CaO_2 might be ascribed to CaO_2-PVP (Fig. 1B). The SEM and TEM results suggest that ZIF-8-CaO_2 presented rhombic dodecahedral morphology consistent with ZIF-8, which further confirmed the XRD results (Fig. 1F and G; Fig. S4, Supporting Information). The nitrogen adsorption-desorption isotherms and pore size distribution indicate that ZIF-8-CaO_2 exhibited the same microporous structure with ZIF-8. However, the specific surface area was reduced by 460 $m^2\,g^{-1}$ compared with ZIF-8, which might be attributed to the presence of CaO_2 inside ZIF-8 as suggested by the broad peak of XRD (Fig. 1C; Table S2, Supporting Information). To further confirm that the CaO_2 was encapsulated by ZIF-8 rather than attached on the surface, the pure ZIF-8 and CaO_2-PVP were mixed to obtain the comparison sample ZIF-8/CaO_2, and the remaining operations were consistent with preparing ZIF-8-CaO_2. TEM was adopted to investigate the existence form of CaO_2. The elemental mapping images of ZIF-8-CaO_2 display the coexistence and homogeneous distribution of C, N, and Zn elements, with Ca element mainly distributed in cavities center (Fig. 1H and I). However, almost no significant Ca element was observed in ZIF-8/CaO_2 (Fig. 1J and K). All of the above characterization results concluded that the ZIF-8 encapsulated CaO_2 nanoparticles were successfully fabricated.

3.2. Preparation and characterization of composite scaffolds

To realize the characteristics of multi-level pore size, customizable structure, and favorable mechanical properties, the 3D printed hydrogel with hybrid double network was fabricated. As shown in Scheme 1, the 3D-printed composite scaffold was obtained by integrating ZIF-8-CaO_2 and hydrogel monomers. The synthesized composite scaffold could provide a suitable microenvironment for angiogenesis and bone regeneration through continuous physical stimulation (multi-level pore size) and chemical intervention (O_2 and ion release).

Acrylamide (AM) was selected as the covalent network monomer because of its good photosensitivity [43]. Sodium carboxymethylcellulose (CC) was chosen as the physical network monomer because of its excellent biocompatibility and adjustable viscosity, which was further cross-linked by Ca^{2+} to form network [44]. Gel scaffold was fabricated by 3D printing bioink composed of the above materials under 405 nm UV light. To obtain the Gel/ZIF-8 and Gel/ZIF-8-CaO_2 composite scaffold, ZIF-8 and ZIF-8-CaO_2 nanoparticles were mixed into the bioink before 3D printing, respectively. As shown in Fig. 2A and B, the Gel scaffold possessed a stable multilayer structure and homogeneous pore


Fig. 2. Physical characterizations of composite scaffolds. A) Digital photograph and B) SEM image of Gel scaffold. C) and D) Magnified SEM images of Gel scaffold. E) Digital photograph and F) SEM image of Gel/ZIF-8-CaO_2 scaffold. G) and H) Magnified SEM images of Gel/ZIF-8-CaO_2 scaffold. I) SEM image and corresponding EDS elemental mapping results of Gel/ZIF-8-CaO_2 scaffold. J) XRD patterns of ZIF-8-CaO_2, Gel, and Gel/ZIF-8-CaO_2. K) O_2 release kinetics of every 2 days of Gel/ZIF-8-CaO_2 scaffold during 14 days. L) Cumulative O_2 release of Gel/ZIF-8-CaO_2 scaffold during 14 days. M) Cumulative Zn^{2+} release of Gel/ZIF-8 and Gel/ZIF-8-CaO_2 scaffolds in SBFs during 28 days. All statistical data are presented as the mean $\pm$ SD (n = 3). *$P < 0.05$, **$P < 0.01$, ***$P < 0.001$.

size of around 500 μm, as did the Gel/ZIF-8-CaO$_2$ scaffold (Fig. 2E and F). The magnified SEM images in Fig. 2C and D reveal the interconnected porous structures within the hydrogel. As shown in Fig. 2G and H, morphologically intact ZIF-8-CaO$_2$ nanoparticles could be clearly observed embedded inside hydrogel without disrupting the internal structure. The microscopic morphology of Gel/ZIF-8 was the same as the Gel/ZIF-8-CaO$_2$ scaffold (Fig. S5, Supporting Information). Moreover, the internal pore sizes of Gel (~9.5 μm), Gel/ZIF-8 (~8.7 μm), and Gel/ZIF-8-CaO$_2$ (~8.2 μm) were similar, further indicating that the introduction of nanoparticles did not affect the cross-linking of hydrogel (Fig. S6, Supporting Information). Meanwhile, the pore structure around 500 μm by 3D printing and the internal pore structure of 8~9 μm constituted the multi-level pore size structure of the scaffold, which can allow cell shuttle and efficient exchange of mineral ions. As illustrated in Fig. 2I, the energy-dispersive spectroscopy elemental scanning analysis was further carried out to assess elemental distribution, which indicated the existence and homogeneous distribution of ZIF-8-CaO$_2$ inside hydrogel. The XRD patterns present the typical peaks of both the Gel and

ZIF-8-CaO$_2$, further confirming the presence of ZIF-8-CaO$_2$ in hydrogel (Fig. 2J). Based on the above results, the Gel/ZIF-8-CaO$_2$ composite scaffold was successfully constructed.

To explore the O$_2$ release capacity, Gel, Gel/CaO$_2$, and Gel/ZIF-8-CaO$_2$ scaffolds were immersed in PBS at 37 °C. We measured the dissolved O$_2$ every 2 days and then the O$_2$ removal operation was carried out after each measurement. Gel/CaO$_2$ exhibited a sudden release of O$_2$ during 2 days and showed no significant difference from the Gel thereafter (Fig. 2K). While the Gel/ZIF-8-CaO$_2$ exhibited a steady and continuous release of O$_2$ during 14 days compared to Gel/CaO$_2$, suggesting the encapsulation effect of ZIF-8. Fig. 2L shows the cumulative O$_2$ release in Gel/ZIF-8-CaO$_2$ scaffold over 14 days. Besides, we measured the release of Zn^{2+} at 37 °C in simulated body fluids to simulate the fluid environment *in vivo*. Fig. 2M illustrates the sustained release of Zn^{2+} in Gel/ZIF-8 and Gel/ZIF-8-CaO$_2$ scaffolds till 4 weeks, which might stimulate angiogenesis and osteogenesis to some extent. Recent study has shown that Zn^{2+} concentrations above 100 μM might suppress vasculogenesis, while below 70 μM could promote HUVECs
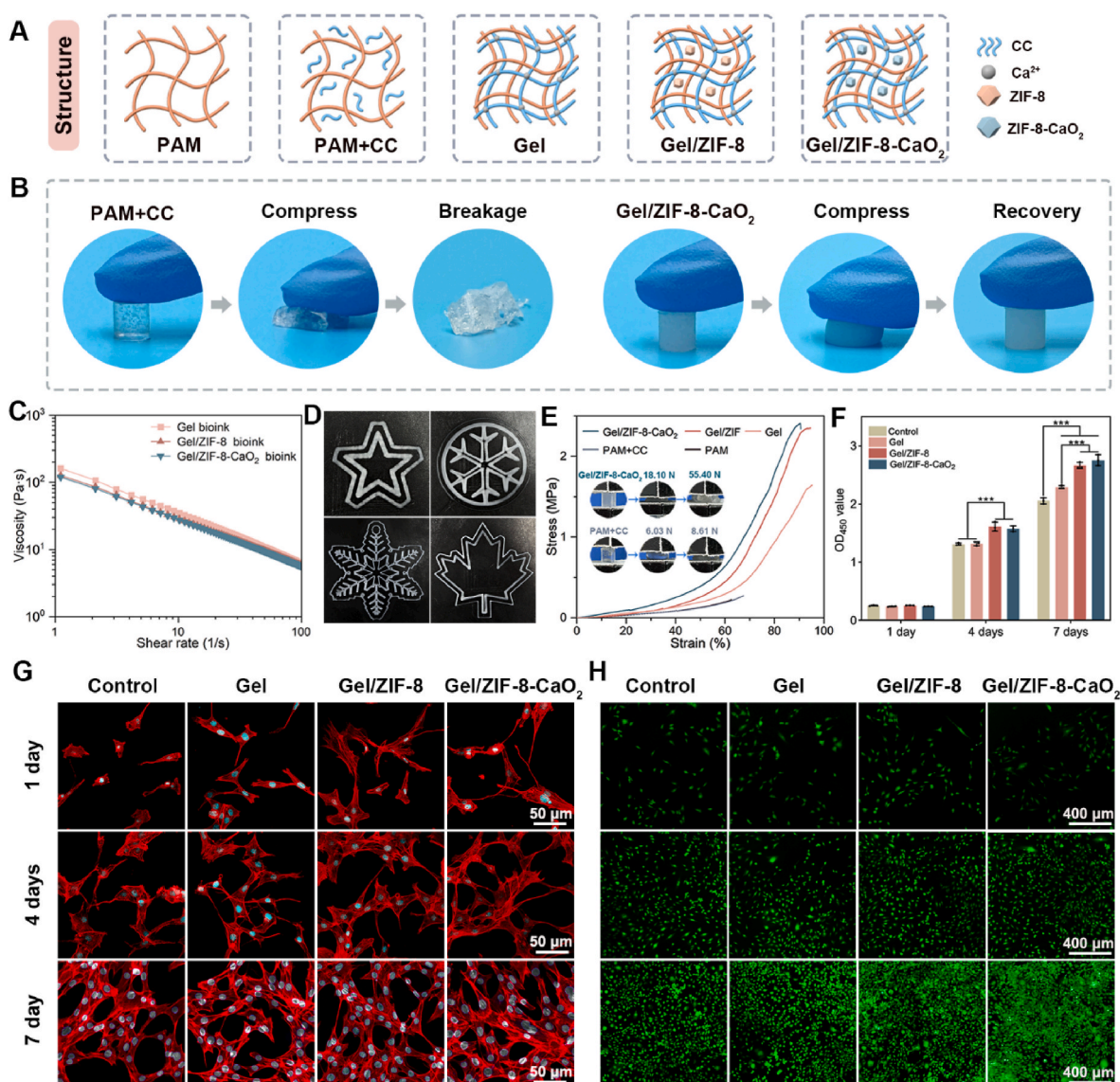
Fig. 3. Mechanical properties, printability, and biocompatibility of composite scaffolds. A) Composition and structure of various scaffolds. B) Digital photographs of PAM + CC and Gel/ZIF-8-CaO$_2$ before and after compression. C) Viscosity vs shear rate sweep curves of different bioinks. D) Gel/ZIF-8-CaO$_2$ proceeded into various shapes by injection molding. E) Compressive stress-strain curve of various scaffolds. F) CCK-8 assay of MC3T3-E1 cells cultured on the scaffolds. G)Morphology of MC3T3-E1 cells on the scaffolds at 1, 4 and 7 days using fluorescence staining (red: cytoskeleton, blue: nuclear). H) Live/dead staining fluorescence images of MC3T3-E1 cells cultured for 1, 4 and 7 days. All statistical data are presented as the mean ± SD (n = 3). *$P < 0.05$, **$P < 0.01$, ***$P < 0.001$.

proliferation [45]. And Zn^{2+} concentration below 57 μg/mL could promote MC3T3-E1 cells proliferation [46]. The concentration of Zn^{2+} released in Gel/ZIF-8 and Gel/ZIF-8-CaO$_2$ was about 0.45 μg/mL (6.92 μM) over 4 weeks, which was within the safe range of promoting cells proliferation.

3.3. Mechanical properties, printability, and biocompatibility of composite scaffolds

Excellent mechanical properties and structural customization are critical for bone-tissue engineering scaffolds. Fig. 3A illustrates the composition and structure of each scaffold. PAM was polymerized by acrylamide to form a covalent network. PAM + CC remained a covalent network structure due to which CC was not cross-linked. After CC was cross-linked by Ca^{2+}, Gel formed a hybrid double network structure. To obtain Gel/ZIF-8 or Gel/ZIF-8-CaO$_2$, ZIF-8 or ZIF-8-CaO$_2$ was added to the monomer mixture. As shown in Fig. 3B, PAM + CC scaffold could be easily crushed because of the brittle single covalent network structure. By contrast, Gel/ZIF-8-CaO$_2$ scaffold was able to recover immediately and retain structural integrity after compression, which exhibited the high toughness owing to the hybrid double network structure. The CC in hydrogel composition imparts bioink injectable property. We synthesized Gel scaffold bioink of different viscosities by adjusting the concentration of CC (The mass ratio of CC to CaCl$_2$ is 1.00, 1.23, and 1.46, respectively). The viscosity of the Gel bioink was too high to stir evenly with the ratio of CC to CaCl$_2$ of 1.46. By reducing the mass ratio to 1.23 or 1.00, the homogeneous Gel bioinks could be obtained. The viscosity of the mass ratio of 1.00 was significantly lower than 1.23, which was not suitable for 3D printing due to its high fluidity (Fig. S7A, Supporting Information). After testing on the 3D printer, the viscosity with a mass ratio of 1.23 was the most appropriate. Then, we prepared bioinks containing ZIF-8 or ZIF-8-CaO$_2$ nanoparticles at this ratio. As shown in Fig. 3C, the addition of ZIF-8 or ZIF-8-CaO$_2$ nanoparticles slightly reduced the viscosity of the bioink, but did not affect subsequent 3D printing. And the viscosity of the bioinks decreased with the increase of shear rate, revealing its shear thinning properties. Remarkably, more diverse and dedicated hydrogel models could be constructed by 3D printing except for the grid-like scaffolds, indicating that the hydrogel possessed outstanding customization performance (Fig. 3D). The compressive strength of the scaffolds was investigated in Fig. 3E and Fig. S7B (Supporting Information). According to the compressive stress-strain curve, the compressive strength of single-network PAM (0.19 MPa) and PAM + CC (0.32 MPa) scaffolds was much lower than that of the Gel (1.64 MPa) scaffold with hybrid double network, which could further confirm that the hybrid double network structure has been successfully fabricated. The intrinsic mechanical strength of single network hydrogels is relatively low. Studies have shown that covalent brittle networks such as PAM break the covalent bonds and cannot recover when an external force is applied [47–49]. The low toughness of the covalent network results in low mechanical strength. Since that the enhancement of their fracture energy is mainly through the dissipation of mechanical energy in the area around the crack, massive mechanical energy can be dissipated when the crack propagates by introducing reversible physical cross-linking to act as a sacrificial bond [50–52]. CC was cross-linked by Ca^{2+} to form a physical network, which shuttled through the covalent network PAM as a sacrificial bond to dissipate energy. The formed hybrid physically–chemically crosslinked network enhanced the toughness and mechanical strength of the hydrogel while achieving self-recovery properties. In addition, the nanoparticles deposited inside the hydrogel could provide strong support in the internal pore structure and achieve high energy dissipation due to the strong interfacial interaction of nanoparticles, which might further improve the mechanical properties of composite hydrogel [53–55]. As expected, the mechanical strength of scaffold was enhanced to 2.34 MPa with the introduction of ZIF-8 or ZIF-8-CaO$_2$ nanoparticles, which were 10 times higher than that of the PAM. Moreover, the compressive

modulus of the Gel/ZIF-8-CaO$_2$ and Gel scaffold sharply increased to 5.92 MPa and 4.98 MPa, respectively, which were 20 times higher than that of the PAM scaffold (0.25 MPa) (Fig. S7C, Supporting Information). The above characterizations demonstrated that the hybrid double network structure endowed the scaffold with excellent mechanical strength and toughness, as well as 3D printability. Therefore, we chose Gel, Gel/ZIF-8, and Gel/ZIF-8-CaO$_2$ for the subsequent vascularized bone regeneration study. Before biocompatibility evaluation, the swelling rate and degradation of various scaffolds were evaluated by immersing in PBS at 37 °C. The scaffolds showed a consistent tendency to reach equilibrium within 8 h, implying that the introduction of nanoparticles did not affect the network structure within scaffolds, which was consistent with the SEM results (Fig. S7D, Supporting Information). All scaffolds incubated in PBS degraded gradually, and the degradation of Gel/ZIF-8 and Gel/ZIF-8-CaO$_2$ was delayed caused by nanoparticle loading (Fig. S7E, Supporting Information). In addition, we studied the release of Ca^{2+} in Gel and Gel/ZIF-8-CaO$_2$ scaffolds (Fig. S7F, Supporting Information). There was no significant difference in Ca^{2+} releasing between the two scaffolds (about 0.13 mg/mL over 21 days) and the trend was similar to that of Gel degradation, indicating that Ca^{2+} was mainly derived from the hydrogel structure.

To assess the biocompatibility of the Gel, Gel/ZIF-8, and Gel/ZIF-8-CaO$_2$ scaffolds, MC3T3-E1 cells were adopted due to the important role in bone regeneration [56]. The quantitative results of CCK-8 assay show that the OD values incremented in control, Gel, Gel/ZIF-8, and Gel/ZIF-8-CaO$_2$ groups after the first day, affirming the positive impact of Zn^{2+} and O$_2$ on cells viability and proliferation (Fig. 3F). We also established the Gel/CaO$_2$ group for cytocompatibility experiment along with other scaffolds. Studies have shown that the sudden release of high level of O$_2$ can damage cells [16,57,58]. The CCK-8 assay results showed that the Gel/CaO$_2$ was cytotoxic, possibly due to the sudden release of high level of O$_2$ (Fig. S8, Supporting Information). However, Gel/ZIF-8-CaO$_2$ showed an obvious cell proliferation effect, which indicated that O$_2$ was no longer suddenly released after encapsulation by ZIF-8. Due to the significant cytotoxicity of unencapsulated CaO$_2$, we would not study Gel/CaO$_2$ scaffold further. As shown in Fig. 3G, the cells could adhere to the various scaffolds surface after co-culturing for 1 day, which might be attributed to the hydrophilic ability of the hydrogel. After co-culturing for 4 days and 7 days, the cells exhibited more spreading and abundant branched filamentous prostheses in Gel/ZIF-8 and Gel/ZIF-8-CaO$_2$ scaffolds, indicating the regulatory function of composite scaffolds on cell adhesion and morphology. To further illustrate the affinity of the scaffolds for cells, we performed Vinculin fluorescent staining, which is often used as a focal adhesion marker [59,60]. Focal adhesions were formed on each scaffold group, indicating that the scaffold had a good affinity for cells due to its hydrophilicity (Fig. S9, Supporting Information). In addition, more focal adhesions were formed in the Gel/ZIF-8 and Gel/ZIF-8-CaO$_2$ groups due to the more stretched cells, suggesting that the composite scaffolds had a promoting effect on the growth of the cells. To further verify the above results, we performed living/dead cell double staining cultured for 1, 4, and 7 days, respectively (Fig. 3H). There was no visible red fluorescence in scaffold groups, which indicated that the scaffolds were no obvious toxicity during the 7-day culture. Moreover, the cell proliferation effect was significantly enhanced with the introduction of ZIF-8 and ZIF-8-CaO$_2$ nanoparticles, which was consistent with the CCK-8 assay and cytoskeleton staining results. These results fully demonstrated that our fabricated scaffolds possessed a satisfactory cytocompatibility, and could significantly promote cell adhesion and proliferation.
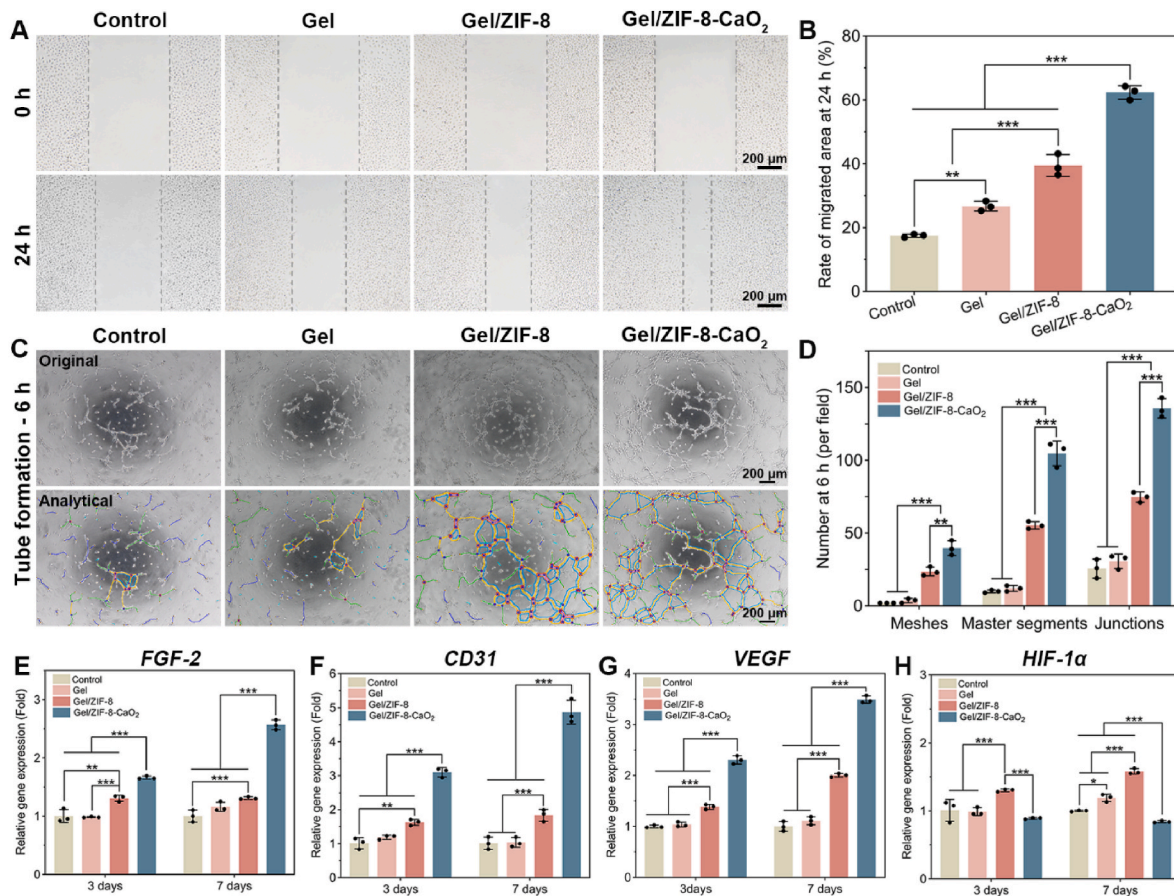
3.4. In vitro angiogenic and osteogenic effect evaluation

Bone regeneration relies on a well-developed blood vessels network to transport essential nutrients and O$_2$ [61]. Thus, the angiogenesis potential of scaffolds was evaluated by co-culturing the HUVECs with various scaffolds extract. The wound healing assay was applied to

estimate the effect of scaffolds on cell migration. All groups appeared migration within 24 h, while the wound closure in Gel/ZIF-8 and Gel/ZIF-8-CaO$_2$ groups was better (Fig. 4A).

Quantitative analysis confirmed the beneficial impact of Zn^{2+} and O$_2$ on HUVECs migration (Fig. 4B). Subsequently, the tube formation assay was performed by incubating HUVECs on Matrigel for 6 h. As shown in Fig. 4C, little tubular network formed in control and Gel groups. In contrast, Gel/ZIF-8 and Gel/ZIF-8-CaO$_2$ groups presented a detailed and well-developed tubular network structure through analytical labeling. The quantitative analysis of mesh, master segment, and junction demonstrated that Zn^{2+} and O$_2$ could effectively facilitate tube formation in HUVECs (Fig. 4D). To further confirm the positive impact of Zn^{2+} and O$_2$, the mRNA expression of angiogenesis-related genes was estimated by quantitative real-time PCR (qRT-PCR) analysis. The Gel/ZIF-8 slightly upregulated the expression of basic fibroblast growth factor (*FGF-2*), platelet endothelial cell adhesion molecule-1 (*CD31*), and vascular endothelial growth factor (*VEGF*) thanks to the released Zn^{2+} (Fig. 4E–G). By further introducing CaO$_2$, the expression of *FGF-2*, *CD31*, and *VEGF* was obviously enhanced in Gel/ZIF-8-CaO$_2$. However, the expression of hypoxia-inducible factor-1 alpha (*HIF-1α*) was downregulated in Gel/ZIF-8-CaO$_2$ compared with other groups, suggesting that the cells were supplied with adequate O$_2$ (Fig. 4H). Overall, these results indicated that Gel/ZIF-8-CaO$_2$ possessed excellent angiogenic potential attributed to the dominance of O$_2$ and the assistance of Zn^{2+}.

Studies found that blood vessels could promote bone formation through coupling with osteogenesis [62]. To verify the osteogenic effect of scaffolds, the activity of alkaline phosphatase (ALP), which plays an important role in early osteogenesis, was detected by staining. As shown in Fig. 5A, the staining intensity and area of ALP in Gel/ZIF-8-CaO$_2$ were significantly greater than other groups in optical pictures and microscopic images analysis. In ARS staining, calcium nodules are stained red to evaluate the mineralized deposition of cells in different groups. We conducted ARS staining on day 14 and performed quantitative analysis (Fig. 5A; Fig. S10, Supporting Information). As a result of culturing with osteoinduction media, visible mineralized nodules were formed in each group. However, the maximum area of mineralization and densification of the distribution of calcium nodules was observed in Gel/ZIF-8-CaO$_2$ group, which was consistent with the results of ALP staining. The mRNA expression of osteogenesis-related genes was also studied (Fig. 5B–E). Bone sialoprotein (*BSP*) is expressed after *ALP*, which can promote nucleation of hydroxyapatite mineralization *in vitro* [63]. Osterix (*OSX*) and bone morphogenetic protein-2 (*BMP-2*) are essential for osteoblast proliferation, differentiation, and bone formation [64,65]. The expression of osteogenesis-related genes in the Gel group was not statistically different from the control, indicating that Ca^{2+} did not play a significant role in osteogenesis in these scaffolds. Studies have found that the concentration of Ca^{2+} between 6 and 15 mM (0.24–0.60 mg/mL) contributes to osteogenic differentiation, while below 6 mM (0.24 mg/mL) cannot significantly promote osteogenic differentiation [66,67]. Therefore, the low concentration of Ca^{2+} released by the scaffolds (0.13 mg/mL) might have no significant effect of osteogenic differentiation. The increased mRNA expression of *BSP*, *OSX*, *BMP-2*, and *ALP* in Gel/ZIF-8 and Gel/ZIF-8-CaO$_2$ groups indicated that the facilitating effect of osteogenic differentiation was mainly due to the released O$_2$ and Zn^{2+}. Combined with the above *in vitro* experimental results, it could be confirmed that the Gel/ZIF-8-CaO$_2$ possessed the dual functions of

Fig. 4. *In vitro* angiogenic effect evaluation of composite scaffolds with HUVECs. A) Optical microscopy images of the wound healing assay at 24 h. B) The quantitative analysis of migrated area in Fig. 4A at 24 h. C) Optical microscopy images of the tube formation assay at 6 h. D) The quantitative analysis of mesh, master segment, and junction of Fig. 4C at 6 h. E-H) Angiogenesis-related genes expression including *FGF-2*, *CD31*, *VEGF* and *HIF-1α* at 3 and 7 days. All statistical data are presented as the mean ± SD (n = 3). *P < 0.05, **P < 0.01, ***P < 0.001.*
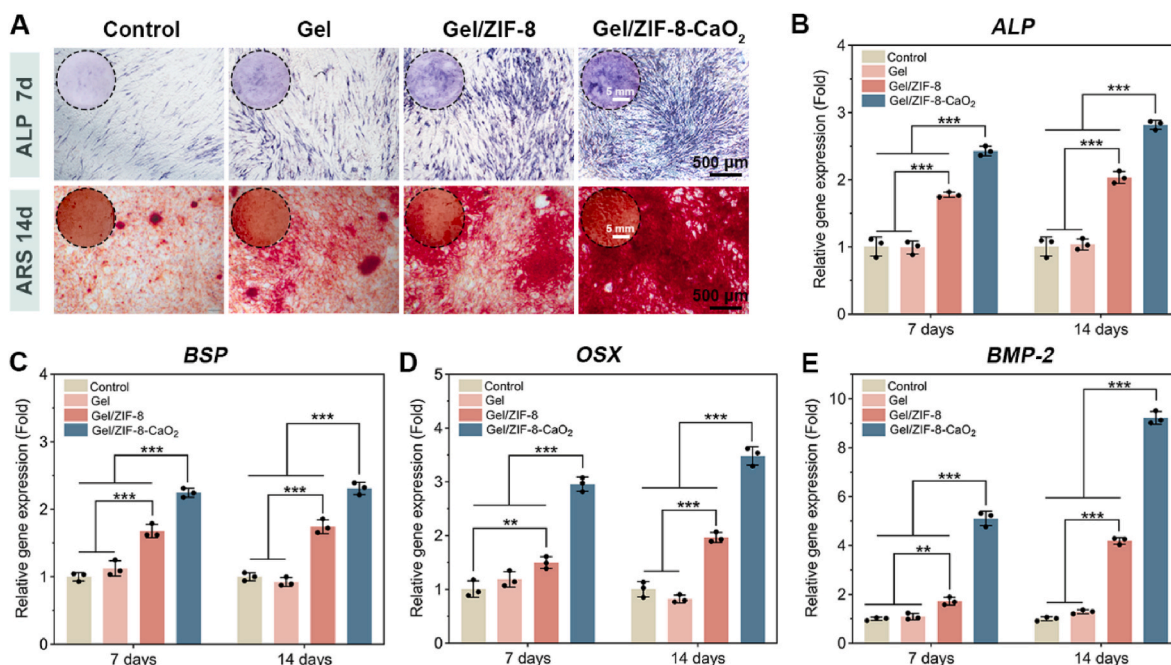
Fig. 5. *In vitro* osteogenic effect evaluation of composite scaffolds with MC3T3-E1 cells. A) General view and optical microscopy images of ALP staining at 7 days and ARS staining at 14 days. B-E) Osteogenesis-related genes expression including *ALP*, *BSP*, *OSX*, and *BMP-2* at 7 and 14 days. All statistical data are presented as the mean ± SD (n = 3). *$P < 0.05$, **$P < 0.01$, ***$P < 0.001$.

stimulating angiogenesis and osteogenesis.
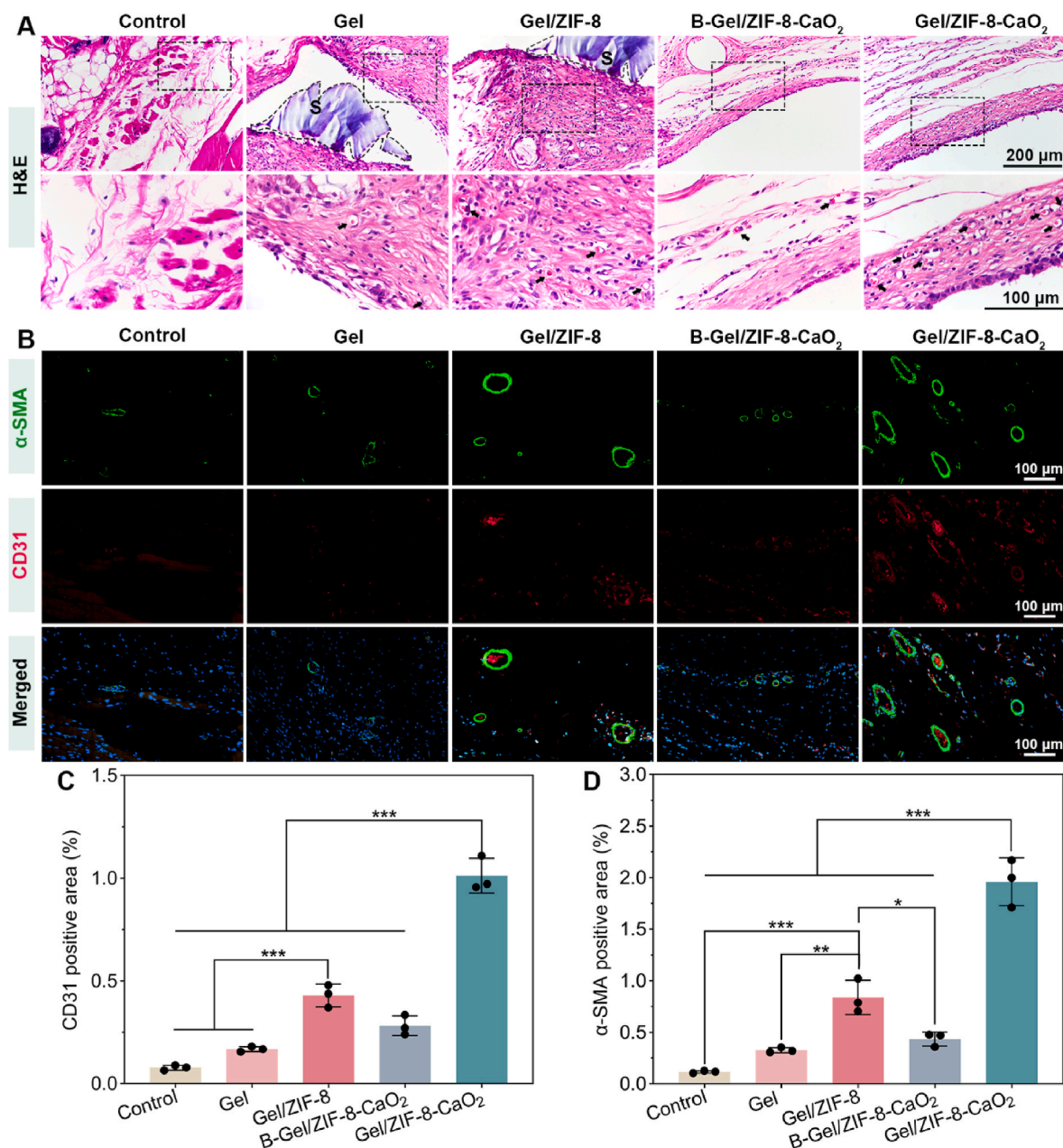
3.5. In vivo angiogenesis evaluation

Rapid vascularization in early stage is key to maintaining tissue viability and accelerating bone regeneration. Subcutaneous implantation was conducted to investigate the effect of scaffolds on early angiogenesis. Besides the control, Gel, Gel/ZIF-8, and Gel/ZIF-8-CaO$_2$, a bulk scaffold without 3D printing treatment (B-Gel/ZIF-8-CaO$_2$) was fabricated to explore the role of 3D printed pore structure. After 14 days of subcutaneous embedding, hematoxylin and eosin (H&E) staining and immunofluorescence staining were performed on the subcutaneous tissue around implanted scaffolds. The results of H&E staining showed that the scaffolds were surrounded by tissue cells, illustrating that the characteristics of extracellular matrix endowed the scaffolds with favorable biocompatibility to facilitate ingrowth of surrounding tissues (Fig. 6A). Besides, the cross-section of neovascularization and the erythrocytes inside (indicated by black arrowheads) could be clearly presented. According to the H&E staining and the results of immunofluorescence, a few newly formed blood vessels could be observed in Gel group, while the expression of CD31 and alpha smooth muscle actin (α-SMA) was weak and no obvious difference from control (Fig. 6B). The quantitative analysis of H&E staining and positively areas in immunofluorescence staining further supported the corresponding conclusions, suggesting that the single effect of 3D printed pore structure was insufficient for angiogenesis (Fig. S11, Supporting Information; Fig. 6C and 6D). The Gel/ZIF-8 promoted angiogenesis with the addition of ZIF-8. The tissues in the H&E staining were normal, indicating that the concentration of released Zn^{2+} was safe and had an angiogenesis-promoting effect. Compared with the introduction of ZIF-8, the addition of ZIF-8-CaO$_2$ further improved the newly formed blood vessels number and the expression levels of CD31 and α-SMA more significantly, which was consistent with the *in vitro* experiment results. Moreover, studies have shown that at least 1–2 weeks of O$_2$ supply is required to effectively promote angiogenesis because the reconstruction of the vascular network takes time [15,68]. The H&E staining showed that the Gel/ZIF-8-CaO$_2$ scaffold had no inflammatory response and no damage

to the surrounding tissues, and the immunofluorescence staining of Gel/ZIF-8-CaO$_2$ scaffold exhibited a significant effect on promoting angiogenesis compared with Gel/ZIF-8. This indicated that the release of O$_2$ from the Gel/ZIF-8-CaO$_2$ scaffold was not sudden and the release time could reach 1–2 weeks to significantly promote angiogenesis *in vivo*. Interestingly, B-Gel/ZIF-8-CaO$_2$ group exhibited inhibition of neovascularization compared with Gel/ZIF-8 and Gel/ZIF-8-CaO$_2$ groups, indicating that 3D-printed pore structure was necessary to exert the effects of O$_2$ and Zn^{2+}. Studies found that pore size of 500 μm possesses optimal cell penetration, which can promote cell infiltration and migration [69]. Therefore, the above findings demonstrated that the synergy of 3D printed pore structure and sustained release of O$_2$ could provide a favorable microenvironment for angiogenesis.

3.6. In vivo bone regeneration evaluation

In light of excellent angiogenic bioactivity *in vivo*, a rat cranial bone defect model was created to ascertain further osteogenesis functionality of Gel/ZIF-8-CaO$_2$ scaffold for 4 and 12 weeks. The results of micro-CT reconstruction display that the scaffold groups formed more new bone in comparison with control (Fig. 7A). In particular, Gel/ZIF-8-CaO$_2$ scaffold generated a large amount of new bone in defect from the edge to the center after 4 weeks of implantation, while Gel/ZIF-8 and B-Gel/ZIF-8-CaO$_2$ groups only showed little new bone formation at the margins. At 12 weeks, more new bone which was still at the edge appeared in Gel/ZIF-8 and B-Gel/ZIF-8-CaO$_2$ groups, while the defect area of Gel/ZIF-8-CaO$_2$ was almost covered by newly formed bone. Meanwhile, the quantitative analysis of specific bone parameters including bone tissue volume/total tissue volume (BV/TV) and trabecular number (Tb.N) shows that Gel/ZIF-8-CaO$_2$ group was obviously higher than other groups (Fig. 7B and C). Based on the above results, the significant promoting effect of Gel/ZIF-8-CaO$_2$ on bone regeneration could be established. Subsequently, H&E staining and Masson's trichrome staining were conducted to further evaluate the condition of the newly formed bone after 4 and 12 weeks of implantation. The control group was filled with fibrous tissue and had almost no new bone formation (Fig. 7D; Fig. S12, Supporting Information). A small amount of new bone bridging

Fig. 6. *In vivo* angiogenesis evaluation in subcutaneous implantation of different scaffolds for 14 days. A) Optical microscopy images of H&E staining (S: scaffold residue, black arrow: newly formed blood vessels). B) Immunofluorescence images of α-SMA (green) and CD31 (red) (cell nucleus: blue). C-D) Quantitative analysis of positive areas of CD31 and α-SMA. All statistical data are presented as the mean ± SD (n = 3). *P < 0.05, **P < 0.01, ***P < 0.001.

the original bone was formed above and under the Gel/ZIF-8 and B-Gel/ZIF-8-CaO₂ scaffolds at 4 weeks., and it tended to grow inward as the scaffolds were gradually degraded over 12 weeks. Surprisingly but within the expectation, the newly formed bone in Gel/ZIF-8-CaO₂ grew toward the scaffold interior at 4 weeks and was almost filled the defect area at 12 weeks, which exhibited prominent osteoconductive and osteoinductive properties. For the Gel/ZIF-8, the cells in the defect center were in a state of long-term hypoxia due to the destruction and untimely reconstruction of vascular network, which could lead to cell viability decrease and even tissue necrosis. As for B-Gel/ZIF-8-CaO₂, the pore structure of 10 μm inside hydrogel could facilitate the efficient exchange of mineral ions and O₂ generated by CaO₂, while it was not conducive to cell ingrowth and proliferation due to the lack of infiltration space. Therefore, the newly formed bone was relatively less and mainly concentrated at the defect edge in Gel/ZIF-8 and B-Gel/ZIF-8-CaO₂ compared with Gel/ZIF-8-CaO₂. By integrating the continuously

generated O₂ and Zn²⁺ with 3D printed pore structure, Gel/ZIF-8-CaO₂ provided a favorable microenvironment for bone regeneration. In addition, the large area vacancy in B-Gel/ZIF-8- CaO₂ at 4 weeks indicated that the bulk hydrogel degraded more slowly than the 3D printed structure in Gel/ZIF-8 and Gel/ZIF-8-CaO₂, which might hinder bone regeneration. At 12 weeks, little scaffold residue was found in Gel/ZIF-8, suggesting that the scaffold biodegradation cycle was long enough to support new bone formation. However, there was no obvious scaffold residue in Gel/ZIF-8-CaO₂ after 12 weeks, indicating that the degradation of scaffold was accelerated by ingrowing bone tissue. Moreover, we performed *in vivo* biosafety testing on major organs including heart, liver, spleen, lung and kidney by H&E staining at 12 weeks (Fig. S13, Supporting Information). The H&E staining results of cranial bone defect model and major organs show no significant histopathological abnormalities in either group, suggesting that the scaffolds are biocompatible.
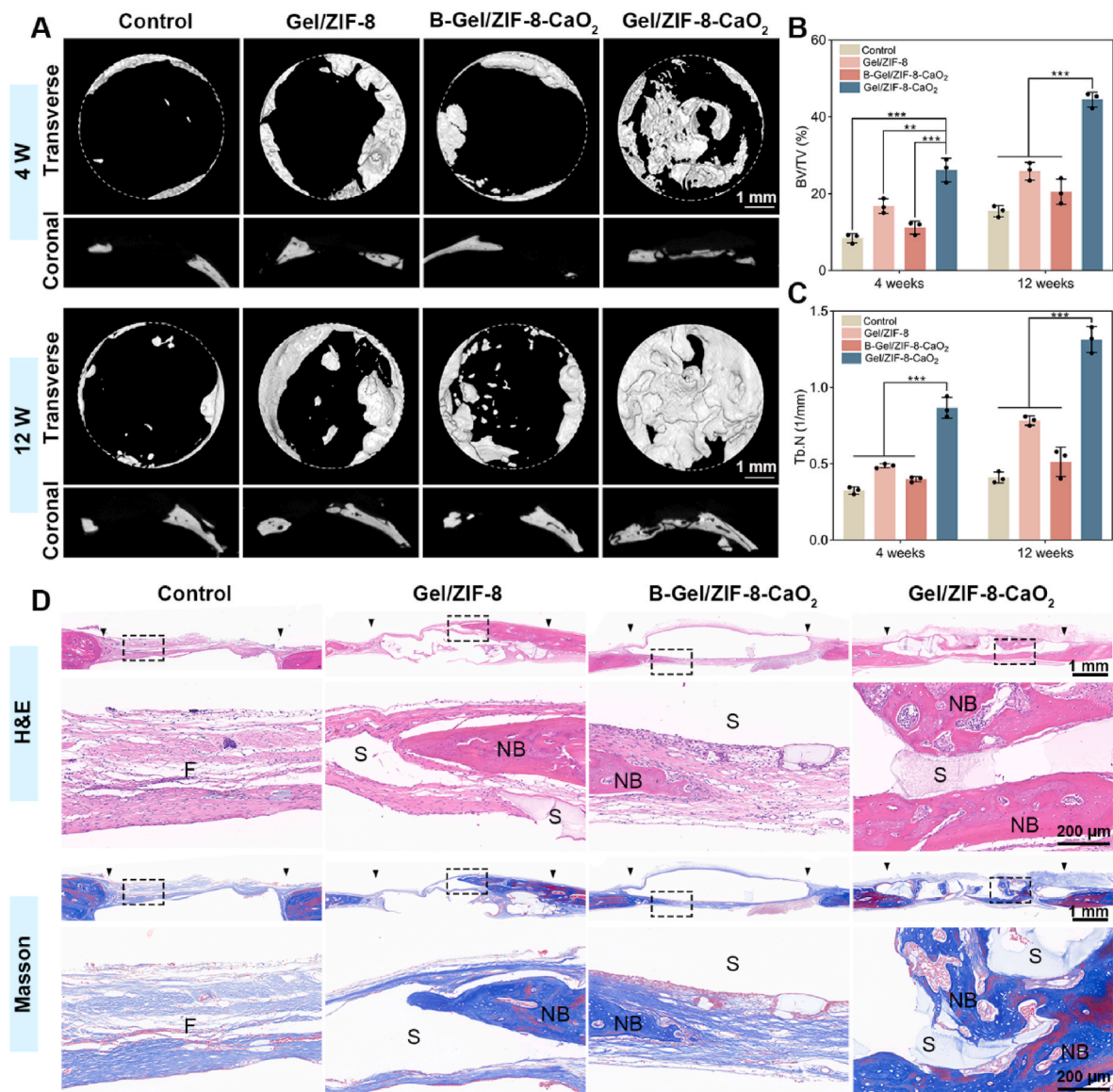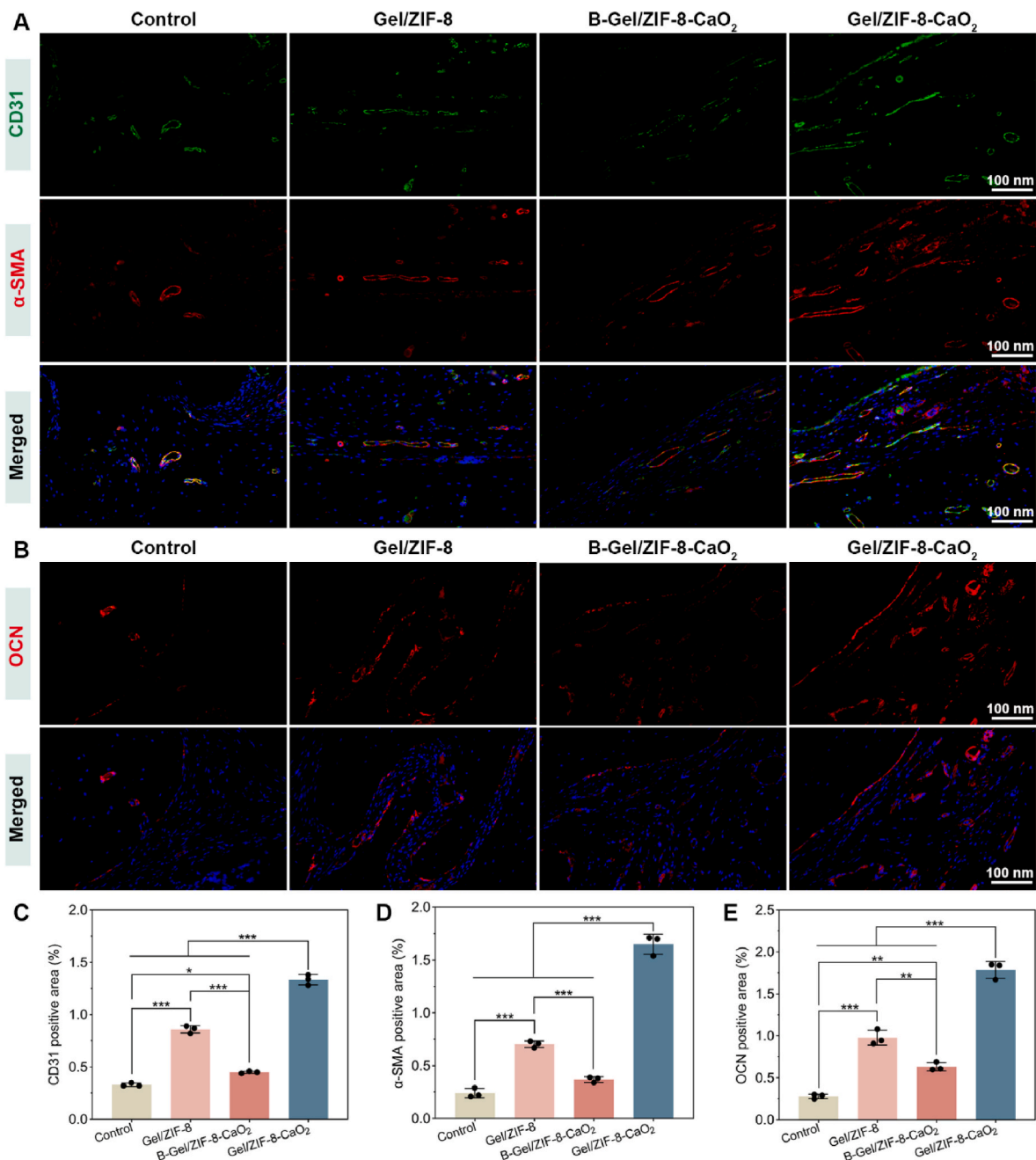
Fig. 7. *In vivo* bone regeneration evaluation in cranial bone defect model of different scaffolds for 4 and 12 weeks. A) Micro-CT images of transverse and coronary section of defect area in different scaffolds after 4 weeks and 12 weeks of regeneration. B–C) Quantitative analysis of BV/TV and Tb.N obtained from micro-CT results. D) H&E staining and Masson staining in different scaffolds for 4 weeks. All statistical data are presented as the mean ± SD (n = 3). *$P < 0.05$, **$P < 0.01$, ***$P < 0.001$.

According to the immunofluorescence staining results of angiogenic marker in Fig. 8A, the expression of CD31 and α-SMA was observed in all groups at 4 weeks. Remarkably, Gel/ZIF-8-CaO$_2$ was verified with the most efficient angiogenesis, as evidenced by the high expression level of CD31 and α-SMA. The quantitative analysis of positive areas further confirmed the above conclusion (Fig. 8C and D). The neovascularization is able to shuttle through the 3D-printed macroporous structure, which can provide enough O$_2$ and nutrients for the osteoblasts to further promote bone regeneration. The significant promotion in OCN expression of Gel/ZIF-8-CaO$_2$ illustrated the importance of the neovascular network for bone regeneration (Fig. 8B and E). Overall, the above results provided convincing evidence that Gel/ZIF-8-CaO$_2$ possessed remarkable functions of promoting bone regeneration through inducing the early angiogenesis.

3.7. Revealing mechanism of osteogenesis based on RNA sequencing

O$_2$ is a crucial factor in cell-to-cell communication, cell proliferation, and cell differentiation as a signaling function. Meanwhile, O$_2$ can upregulate the expression of vascular endothelial growth factor for the promotion of angiogenesis and further regulate osteogenesis [70–72]. Gel/ZIF-8-CaO$_2$ scaffold exhibited the best angiogenesis and osteogenic abilities based on *in vitro* and *in vivo* experimental results, which was attributed to the O$_2$ released. We performed RNA-seq assay for Gel/ZIF-8 and Gel/ZIF-8-CaO$_2$ scaffolds to further reveal the underlying mechanisms of O$_2$-promoted osteogenesis. The volcano plot displayed 557 up-regulated and 682 down-regulated differentially expressed genes (DEGs) (Fig. 9A). Gene ontology (GO) enrichment analysis of DEGs showed significant upregulation in the aspects of cell viability and adhesion (positive regulation of cell motility, positive regulation of cell adhesion, positive regulation of cell activation, etc.), cell proliferation and migration (smooth muscle cell migration, positive regulation of smooth muscle cell proliferation, positive regulation of cell migration, etc.), extracellular matrix organization (extracellular matrix binding, collagen biosynthetic process), angiogenesis (angiogenesis, positive regulation of vasculature development, VEGF signaling pathway, etc.),

Fig. 8. Histological evaluations of angiogenesis and bone regeneration in cranial bone defect model. A) Fluorescence images of CD31 (green) and α-SMA (red) (cell nucleus: blue). B) Fluorescence images of OCN (red) (cell nucleus: blue). C-E) Quantitative analysis of CD31, α-SMA, and OCN. All statistical data are presented as the mean ± SD (n = 3). *$P < 0.05$, **$P < 0.01$, ***$P < 0.001$.*

and osteogenic differentiation (biomineral tissue development, positive regulation of ossification, positive regulation of osteoblast differentiation, etc.) (Fig. 9B). Moreover, the transforming growth factor-β (TGF-β) pathway and p38 mitogen-activated protein kinase (p38MAPK) cascade were also significantly enriched, which were closely related to the osteogenesis [73–75]. We further analyzed the important enrichment pathways for vascular and osteogenic differentiation by GESA (Fig. 9C).

We enriched DEGs by Kyoto Encyclopedia of Genes and Genomes (KEGG) database and the top 25 enriched KEGG pathways were presented in Fig. 9D. The pathways including the aspects of cell adhesion (Rap1 signaling pathway, Focal adhesion) and proliferation (cell cycle, ECM-receptor interaction, FoxO signaling pathway) were identified. Furthermore, TGF-β and MAPK pathways were also observed, which was consistent with the GO results. It has been shown that TGF-β can not only

control the proliferation and differentiation of osteoblasts by affecting cell division and proliferation, but also activate the MAPK pathway to induce osteoblast differentiation and proliferation [76–78]. In addition, they can synthesize extracellular matrices containing *OCN* and *BMP*-2 by the induction of osteoblasts, which further promotes matrix mineralization [79]. We performed heat map analysis of highly expressed DEGs (Fig. 9E), including the aspects of cell proliferation and differentiation (*Ghr*, *Emp3*, etc.), extracellular matrix (*Dmp1*, *Spp1*, etc.), angiogenesis (*Vegfa*, *Pgk1-rs7*, etc.), and osteogenesis (*Tlr2*, *Lrrc15*, etc.). Moreover, it was reported that the upregulation of *Id4*, *Dcn*, *Myc*, *Mapk3*, *Atf4*, etc. was observed in the TGF-β pathway and MAPK pathway activated by TGF-β, and they could promote the expression of osteogenesis-related genes including *BMP-2*, *ALP*, *OCN* and *OSX*, which was confirmed by the above qRT-PCR and fluorescent staining results
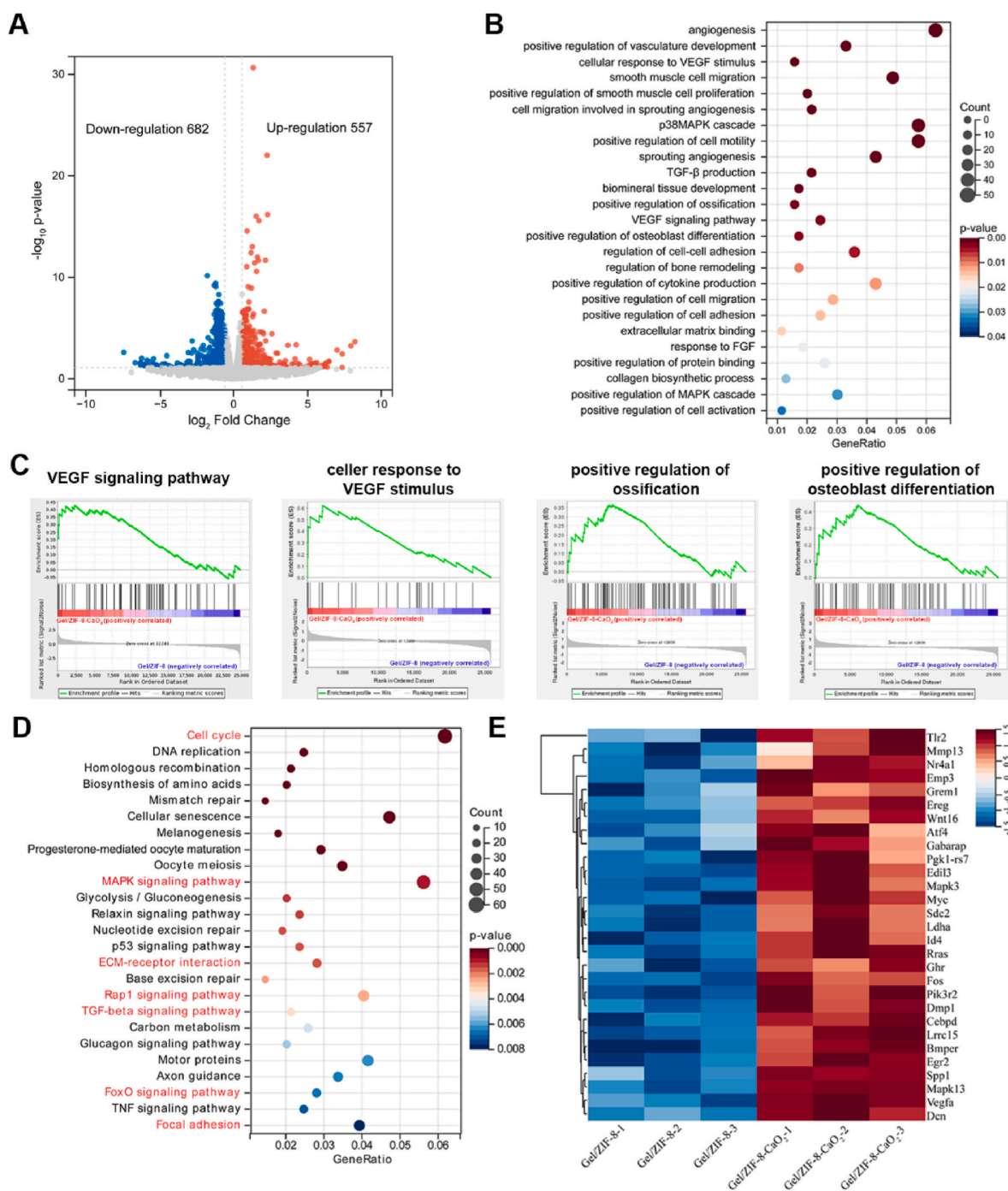
Fig. 9. Gel/ZIF-8-CaO$_2$ scaffold regulates pathway expressions related to osteogenesis and angiogenesis. A) Volcano plot of the differentially expressed genes (DEGs) from Gel/ZIF-8-CaO$_2$ versus Gel/ZIF-8. B) Representative 25 enriched GO up terms of DEGs from Gel/ZIF-8-CaO$_2$ versus Gel/ZIF-8. C) GSEA plots of Gel/ZIF-8-CaO$_2$ versus Gel/ZIF-8. D) Top 25 results from the enriched KEGG pathways of DEGs from Gel/ZIF-8-CaO$_2$ versus Gel/ZIF-8. E) Heatmap of DEGs related to cellular activity, angiogenesis and osteogenesis from Gel/ZIF-8-CaO$_2$ versus Gel/ZIF-8.

[80–85]. Together, the RNA-seq results were consistent with the above *in vitro* and *in vivo* experimental results, which revealed that the Gel/-ZIF-8-CaO$_2$ scaffold might first enhance cell adhesion, proliferation and differentiation, and then complete the composition of the extracellular matrix, further promote angiogenesis and osteogenesis by releasing O$_2$.

4. Conclusions

In conclusion, we have successfully developed a Gel/ZIF-8-CaO$_2$ composite hydrogel scaffold from the perspective of constructing a favorable microenvironment for augmented vascularized bone regeneration without the aid of cells or growth factors. The scaffold was capable of releasing O$_2$ in a steady and sustained manner by CaO$_2$ nanoparticles encapsulated in ZIF-8. By constructing the hybrid double network hydrogel structure, the scaffold exhibited excellent mechanical strength, which was 10 times greater than that of single network hydrogel. In addition, the fast-curing and extrusible precursor made the hydrogel 3D printable, thus repairing the irregular bone defects. *In vitro* and *in vivo* experiments results demonstrated that the releasing O$_2$ promoted cell proliferation and differentiation, perfected extracellular

matrix organization, and initiated rapid angiogenesis and osteogenesis. *In vivo* results suggested that the synergy of O_2 and 3D printed pore structure significantly stimulated rapid reconstruction of early vascular network in 2 weeks and achieve bone regeneration in all areas of the defect in 12 weeks with the assistance of Zn^{2+}, displaying superior osteoconductive and osteoinductive properties. This strategy might provide inspiration for the development of cell/factor-free scaffolds that enhance angiogenesis and osteogenesis, which is expected to be a potential clinical alternative.

Ethics approval and consent to participate

All animal experiments were approved by the Animal Care and Welfare Committee of Tianjin Nankai Hospital (Approval No. NKYY-DWLL-2023-066), and performed in compliance with the Guidelines for Care and Use of Laboratory Animals.

CRediT authorship contribution statement

Yang Yang: Writing – original draft, Methodology, Investigation, Conceptualization. **Wanmeng Wang:** Resources, Formal analysis. **Qianrui Zeng:** Investigation, Formal analysis. **Ning Wang:** Resources. **Wenbo Li:** Investigation. **Bo Chen:** Funding acquisition, Conceptualization. **Qingxin Guan:** Supervision, Funding acquisition, Conceptualization. **Changyi Li:** Supervision, Funding acquisition. **Wei Li:** Supervision, Funding acquisition, Conceptualization.

Declaration of competing interest

The authors declare that they have no known competing financial interests or personal relationships that could have appeared to influence the work reported in this paper.

Acknowledgements

Appendix A. Supplementary data

Supplementary data to this article can be found online at https://doi.org/10.1016/j.bioactmat.2024.06.016.

References

[1] J. Zhang, D. Tong, H. Song, R. Ruan, Y. Sun, Y. Lin, J. Wang, L. Hou, J. Dai, J. Ding, H. Yang, Osteoimmunity-regulating Biomimetically Hierarchical scaffold for augmented bone regeneration, Adv. Mater. 34 (36) (2022), https://doi.org/10.1002/adma.202202044.

[2] Y. Ha, X. Ma, S. Li, T. Li, Z. Li, Y. Qian, M. Shafiq, J. Wang, X. Zhou, C. He, Bone microenvironment-Mimetic scaffolds with Hierarchical Microstructure for enhanced vascularization and bone regeneration, Adv. Funct. Mater. 32 (20) (2022) 2200011, https://doi.org/10.1002/adfm.202200011.

[3] G. Lu, Y. Xu, Q. Liu, M. Chen, H. Sun, P. Wang, X. Li, Y. Wang, X. Li, X. Hui, E. Luo, J. Liu, Q. Jiang, J. Liang, Y. Fan, Y. Sun, X. Zhang, An Instantly fixable and self-Adaptive scaffold for skull regeneration by autologous stem cell Recruitment and angiogenesis, Nat. Commun. 13 (1) (2022) 2499, https://doi.org/10.1038/s41467-022-30243-5.

[4] S. Liu, L. Zhang, Z. Li, F. Gao, Q. Zhang, A. Bianco, H. Liu, S. Ge, B. Ma, Materials-Mediated in situ physical Cues for bone regeneration, Adv. Funct. Mater. 34 (1) (2023), https://doi.org/10.1002/adfm.202306534.

[5] M. Gholipourmalekabadi, S. Zhao, B. Harrison, M. Mozafari, A. Seifalian, Oxygen-generating biomaterials: a new, viable Paradigm for tissue engineering? Trends Biotechnol. 34 (12) (2016) 1010–1021, https://doi.org/10.1016/j.tibtech.2016.05.012.

[6] S. Suvarnapathaki, X. Wu, D. Lantigua, M. Nguyen, G. Camci-Unal, Breathing Life into engineered tissues using oxygen-releasing biomaterials, NPG Asia Mater. 11 (1) (2019), https://doi.org/10.1038/s41427-019-0166-2.

[7] S. Yin, W. Zhang, Z. Zhang, X. Jiang, Recent Advances in scaffold Design and material for vascularized tissue-engineered bone regeneration, Adv. Healthcare Mater. 8 (10) (2019), https://doi.org/10.1002/adhm.201801433.

[8] M. Touri, F. Moztarzadeh, N. Osman, M. Dehghan, M. Mozafari, 3D-Printed Biphasic calcium phosphate scaffolds Coated with an oxygen generating System for enhancing engineered tissue survival, Mater. Sci. Eng., C 84 (2018) 236–242, https://doi.org/10.1016/j.msec.2017.11.037.

[9] H. Kim, S. Kim, H. Lee, J. Lee, G. Rho, H. Lee, H. Lee, J. Byun, S. Oh, Oxygen-releasing Microparticles for cell survival and differentiation ability under hypoxia for effective bone regeneration, Biomacromolecules 20 (2) (2019) 1087–1097, https://doi.org/10.1021/acs.biomac.8b01760.

[10] D. Mayer, K. Ferenz, Perfluorocarbons for the treatment of Decompression Illness: How to Bridge the Gap between theory and Practice, Eur. J. Appl. Physiol. 119 (2019) 2421–2433, https://doi.org/10.1007/s00421-019-04252-0.

[11] V. Centis, P. Proulx, P. Vermette, PEGylated Liposomes encapsulating Human Hemoglobin enhance oxygen transfer and cell proliferation while decreasing cell hypoxia in Fibrin, Biochem. Eng. J. 55 (3) (2011) 162–168, https://doi.org/10.1016/j.bej.2011.04.001.

[12] C. Wang, H. Xu, C. Liu, Z. Peng, R. Min, Z. Zhang, J. Li, Y. Jin, Y. Wang, Z. Li, J. Guo, L. Zhu, CaO_2/Gelatin oxygen Slow-releasing microspheres facilitate tissue engineering efficiency for the Osteonecrosis of Femoral Head by enhancing the angiogenesis and survival of grafted bone Marrow Mesenchymal stem cells, Biomater. Sci. 9 (8) (2021) 3005–3018, https://doi.org/10.1039/d0bm02071k.

[13] M. Touri, F. Moztarzadeh, N. Osman, M. Dehghan, P. Brouki Milan, S. Farzad-Mohajeri, M. Mozafari, Oxygen-releasing scaffolds for accelerated bone regeneration, ACS Biomater. Sci. Eng. 6 (5) (2020) 2985–2994, https://doi.org/10.1021/acsbiomaterials.9b01789.

[14] C. Gao, Y. Huang, L. Zhang, P. Wei, W. Jing, H. Wang, Z. Yuan, D. Zhang, Y. Yu, X. Yang, Q. Cai, Self-reinforcement hydrogel with sustainable oxygen-supply for enhanced cell ingrowth and potential tissue regeneration, Biomater. Adv. 141 (2022), https://doi.org/10.1016/j.bioadv.2022.213105.

[15] N. Ashammakhi, M. Darabi, N. Kehr, A. Erdem, S. Hu, M. Dokmeci, A. Nasr, A. Khademhosseini, Advances in Controlled oxygen generating biomaterials for tissue engineering and regenerative Therapy, Biomacromolecules 21 (1) (2019) 56–72, https://doi.org/10.1021/acs.biomac.9b00546.

[16] S. Suvarnapathaki, X. Wu, T. Zhang, M. Nguyen, A. Goulopoulos, B. Wu, Oxygen generating scaffolds regenerate critical size bone defects, Bioact. Mater. 13 (2022) 64–81, https://doi.org/10.1016/j.bioactmat.2021.11.002.

[17] Y. Sun, L. Zheng, Y. Yang, X. Qian, T. Fu, X. Li, Z. Yang, H. Yan, C. Cui, W. Tan, Metal–organic framework Nanocarriers for drug delivery in Biomedical applications, Nano-Micro Lett. 12 (1) (2020) 103, https://doi.org/10.1007/s40820-020-00423-3.

[18] F. Lyu, Y. Zhang, R. Zare, J. Ge, Z. Liu, One-pot synthesis of protein-embedded metal–organic frameworks with enhanced Biological Activities, Nano Lett. 14 (10) (2014) 5761–5765, https://doi.org/10.1021/nl5026419.

[19] N. Abbasi, S. Hamlet, R. Love, N. Nguyen, Porous scaffolds for bone regeneration, J. Sci.-Adv. Mater. Dev. 5 (1) (2020) 1–9, https://doi.org/10.1016/j.jsamd.2020.01.007.

[20] V. Karageorgiou, D. Kaplan, Oxygen generating scaffolds regenerate critical size bone defects, Biomaterials 26 (27) (2005) 5474–5491, https://doi.org/10.1016/j.biomaterials.2005.02.002.

[21] J. Temple, D. Hutton, B. Hung, P. Huri, C. Cook, R. Kondragunta, X. Jia, W. Grayson, Engineering Anatomically shaped vascularized bone grafts with hASCs and 3D-printed PCL scaffolds, J. Biomed. Mater. Res. 102A (2014), https://doi.org/10.1002/jbm.a.35107.

[22] X. Bai, M. Gao, S. Syed, J. Zhuang, X. Xu, X. Zhang, Bioactive hydrogels for bone regeneration, Bioact. Mater. 3 (4) (2018) 401–417, https://doi.org/10.1016/j.bioactmat.2018.05.006.

[23] L. Wu, X. Pei, B. Zhang, Z. Su, X. Gui, C. Gao, L. Guo, H. Fan, Q. Jiang, L. Zhao, C. Zhou, Y. Fan, X. Zhang, 3D-Printed HAp bone regeneration scaffolds enable Nano-scale Manipulation of cellular Mechanotransduction Signals, Chem. Eng. J. 455 (2023) 140699, https://doi.org/10.1016/j.cej.2022.140699.

[24] C. Yang, H. Ma, Z. Wang, M. Younis, C. Liu, C. Wu, Y. Luo, P. Huang, 3D printed Wesselsite Nanosheets Functionalized scaffold facilitates NIR-II Photothermal Therapy and vascularized bone regeneration, Adv. Sci. 8 (20) (2021) 2100894, https://doi.org/10.1002/advs.202100894.

[25] T. Arinzeh, T. Tran, J. McAlary, G. Daculsi, A Comparative study of Biphasic calcium phosphate Ceramics for Human Mesenchymal stem-cell-induced bone formation, Biomaterials 26 (17) (2005) 3631–3638, https://doi.org/10.1016/j.biomaterials.2004.09.035.

[26] D. Wang, Y. Wang, D. Song, B. Bai, Y. Ci, Z. Gong, Y. Hua, X. Wang, G. Zhou, Microgels-encapsulated Magnesium/Emodin-based metal organic framework Nanorods for Diabetic bone regeneration, Chem. Eng. J. 487 (2024) 150585, https://doi.org/10.1016/j.cej.2024.150585.

[27] B. Bai, Y. Liu, J. Huang, S. Wang, H. Chen, Y. Huo, H. Zhou, Y. Liu, S. Feng, G. Zhou, Y. Hua, Tolerant and rapid Endochondral bone regeneration using Framework-enhanced 3D Biomineralized matrix hydrogels, Adv. Sci. 11 (9) (2023) 2305580, https://doi.org/10.1002/advs.202305580.

[28] B. Maharjan, J. Park, V. Kaliannagounder, G. Awasthi, M. Joshi, C. Park, C. Kim, Regenerated Cellulose Nanofiber Reinforced Chitosan hydrogel scaffolds for bone tissue Eengineering, Carbohydr. Polym. 251 (2021), https://doi.org/10.1016/j.carbpol.2020.117023.

[29] W. Kim, H. Lee, E. Roh, S. An, I. Han, G. Kim, A Multicellular Bioprinted cell construct for vascularized bone tissue regeneration, Chem. Eng. J. 431 (2022) 133882, https://doi.org/10.1016/j.cej.2021.133882.

[30] G. Ingavle, M. Gionet-Gonzales, C. Vorwald, L. Bohannon, K. Clark, L. Galuppo, J. Leach, Injectable mineralized Microsphere-loaded composite hydrogels for bone repair in a Sheep bone defect model, Biomaterials 197 (2019) 119–128, https://doi.org/10.1016/j.biomaterials.2019.01.005.

[31] L. Wang, D. Li, Y. Huang, R. Mao, B. Zhang, F. Luo, P. Gu, P. Song, X. Ge, J. Lu, X. Yang, Y. Fan, X. Zhang, K. Wang, Bionic mineralized 3D-printed scaffolds with enhanced in situ mineralization for cranial bone regeneration, Adv. Funct. Mater. 34 (2023) 2309042, https://doi.org/10.1002/adfm.202309042.

[32] J. Tao, S. Zhu, X. Liao, Y. Wang, N. Zhou, Z. Li, H. Wan, Y. Tang, S. Yang, T. Du, Y. Yang, J. Song, R. Liu, DLP-Based Bioprinting of Void-forming hydrogels for enhanced stem-cell-mediated bone regeneration, Mater. Today Bio 17 (2022) 100487, https://doi.org/10.1016/j.mtbio.2022.100487.

[33] T. Nakajima, Y. Tanaka, T. Kurokawa, Y. Osada, J. Gong, True chemical structure of double network hydrogels, Macromolecules 42 (6) (2009) 2184–2189, https://doi.org/10.1021/ma802148p.

[34] J. Gong, Y. Katsuyama, T. Kurokawa, Y. Osada, Double-network hydrogels with Extremely high mechanical strength, Adv. Mater. 15 (14) (2003) 1155–1158, https://doi.org/10.1002/adma.200304907.

[35] L. Che, Z. Lei, P. Wu, D. Song, A 3D printable and bioactive hydrogel scaffold to Treat Traumatic Brain Injury, Adv. Funct. Mater. 29 (39) (2019), https://doi.org/10.1002/adfm.201904450.

[36] H. Zhang, H. Huang, G. Hao, Y. Zhang, H. Ding, Z. Fan, L. Sun, 3D printing hydrogel scaffolds with Nanohydroxyapatite Gradient to effectively repair Osteochondral defects in rats, Adv. Funct. Mater. 31 (1) (2020), https://doi.org/10.1002/adfm.202006697.

[37] X. Zhang, K. Wang, J. Hu, Y. Zhang, Y. Dai, F. Xia, Role of a high calcium ion content in Extending the properties of alginate dual-crosslinked hydrogels, J. Mater. 8 (47) (2020) 25390–25401, https://doi.org/10.1039/d0ta09315g.

[38] B. Wang, W. Zhang, Q. Pan, J. Tao, S. Li, T. Jiang, X. Zhao, Hyaluronic acid-based CuS Nanoenzyme biodegradable Microneedles for treating Deep Cutaneous Fungal Infection without drug Resistance, Nano Lett. 23 (4) (2023) 1327–1336, https://doi.org/10.1021/acs.nanolett.2c04539.

[39] J. Zhuang, A. Young, C. Tsung, Integration of Biomolecules with metal–organic frameworks, Small 13 (32) (2017), https://doi.org/10.1002/smll.201700880.

[40] X. Huang, D. Huang, T. Zhu, X. Yu, K. Xu, H. Li, H. Qu, Z. Zhou, K. Cheng, W. Wen, Z. Ye, Sustained zinc release in Cooperation with CaP scaffold promoted bone regeneration via directing stem cell fate and Triggering a Pro-healing Immune Stimuli, J. Nanobiotechnol. 19 (1) (2021), https://doi.org/10.1186/s12951-021-00956-8.

[41] G. Lu, S. Li, Z. Guo, O. Farha, B. Hauser, X. Qi, Y. Wang, X. Wang, S. Han, X. Liu, J. DuChene, H. Zhang, Q. Zhang, X. Chen, J. Ma, S. Soo, W. Wei, Y. Yang, J. Hupp, F. Huo, Imparting functionality to a metal–organic framework material by Controlled nanoparticle encapsulation, Nat. Chem. 4 (4) (2012) 310–316, https://doi.org/10.1038/nchem.1272.

[42] S. Shen, M. Mamat, S. Zhang, J. Cao, Z. Hood, L. Figueroa-Cosme, Y. Xia, Synthesis of CaO₂ Nanocrystals and their spherical Aggregates with uniform sizes for Use as a biodegradable Bacteriostatic agent, Small 15 (36) (2019) 1902118, https://doi.org/10.1002/smll.201902118.

[43] A. Kumar, K. Rao, S. Han, Mechanically Viscoelastic Nanoreinforced hybrid hydrogels composed of polyacrylamide, sodium carboxymethylcellulose, Graphene oxide, and Cellulose Nanocrystals, Carbohydr. Polym. 193 (2018) 228–238, https://doi.org/10.1016/j.carbpol.2018.04.004.

[44] T. Elkins, R. Bury, J. Ritter, F. Ling, R. Ahokas, C. Homsey, L. Russell Malinak, Adhesion prevention by solutions of sodium carboxymethylcellulose in the rat. I, Fertil. Steril. 41 (6) (1984) 926–928, https://doi.org/10.1016/s0015-0282(16)47909-4.

[45] Y. Wang, N. Huang, Z. Yang, Revealing the role of zinc ions in Atherosclerosis Therapy via an engineered three-Dimensional Pathological model, Adv. Sci. 10 (18) (2023) 2300475, https://doi.org/10.1002/advs.202300475.

[46] Y. Meng, M. Yang, X. Liu, W. Yu, B. Yang, Zn²⁺-Doped Carbon Dots, a good biocompatibility nanomaterial applied for Bio-Imaging and inducing osteoblastic differentiation in vitro, Nano 14 (3) (2019) 1950029, https://doi.org/10.1142/s1793292019500292.

[47] L. Li, P. Wu, F. Yu, J. Ma, Double network hydrogels for energy/Environmental applications: Challenges and Opportunities, J. Mater. 10 (17) (2022) 9215–9247, https://doi.org/10.1039/d2ta00540a.

[48] X. Xu, V. Jerca, R. Hoogenboom, Bioinspired double network Hdrogels: from covalent double network hydrogels via hybrid double network hydrogels to physical double network hydrogels, Mater. Horiz. 8 (4) (2021) 1173–1188, https://doi.org/10.1039/d0mh01514h.

[49] F. Ullah, M. Othman, F. Javed, Z. Ahmad, H. Akil, Classification, processing and application of hydrogels: a review, Mater. Sci. Eng. C 57 (2015) 414–433, https://doi.org/10.1016/j.msec.2015.07.053.

[50] C. Peak, J. Wilker, G. Schmidt, A review on Tough and Sticky hydrogels, Colloid Polym. Sci. 291 (9) (2013) 2031–2047, https://doi.org/10.1007/s00396-013-3021-y.

[51] X. Zhao, Multi-scale multi-mechanism Design of Tough hydrogels: Building dissipation into Stretchy networks, Soft Matter 10 (5) (2014) 672–687, https://doi.org/10.1039/c3sm52272e.

[52] J. Sun, X. Zhao, W. Illeperuma, O. Chaudhuri, K. Oh, D. Mooney, J. Vlassak, Z. Suo, Highly stretchable and Tough hydrogels, Nature 489 (7414) (2012) 133–136, https://doi.org/10.1038/nature11409.

[53] J. Fang, P. Li, X. Lu, L. Fang, X. Lü, F. Ren, A strong, Tough, and osteoconductive hydroxyapatite mineralized polyacrylamide/Dextran hydrogel for bone tissue regeneration, Acta Biomater. 88 (2019) 503–513, https://doi.org/10.1016/j.actbio.2019.02.019.

[54] R. Kane, H. Weiss-Bilka, M. Meagher, Y. Liu, J. Gargac, G. Niebur, D. Wagner, R. Roeder, Hydroxyapatite Reinforced collagen scaffolds with improved architecture and mechanical properties, Acta Biomater. 17 (2015) 16–25, https://doi.org/10.1016/j.actbio.2015.01.031.

[55] R. Roeder, G. Converse, R. Kane, W. Yue, Hydroxyapatite-reinforced polymer Biocomposites for synthetic bone Substitutes, JOM (J. Occup. Med.) 60 (2008) 30–45, https://doi.org/10.1007/s11837-008-0030-2.

[56] Y. Wu, X. Li, Y. Sun, X. Tan, C. Wang, Z. Wang, L. Ye, Multiscale Design of Stiffening and ROS Scavenging hydrogels for the Augmentation of Mandibular bone regeneration, Bioact. Mater. 20 (2023) 111–125, https://doi.org/10.1016/j.bioactmat.2022.05.021.

[57] A. Baik, A. Haribowo, X. Chen, B. Queliconi, A. Barrios, A. Garg, M. Maishan, A. Campos, M. Matthay, I. Jain, Oxygen toxicity causes cyclic damage by Destabilizing specific Fe-S Cluster-containing protein Complexes, Mol. Cell 83 (6) (2023) 942–960, https://doi.org/10.1016/j.molcel.2023.02.013.

[58] A. Alayash, Hemoglobin-based blood Substitutes and the treatment of Sickle cell disease: more Harm than help? Biomolecules 7 (4) (2017) https://doi.org/10.3390/biom7010002.

[59] L. Chu, G. Jiang, X. Hu, T. James, X. He, Y. Li, T. Tang, Biodegradable macroporous scaffold with Nano-crystal surface Microstructure for highly effective osteogenesis and vascularization, J. Mater. Chem. B 6 (11) (2018) 1658–1667, https://doi.org/10.1039/c7tb03353b.

[60] L. Chu, Y. Yang, S. Yang, Q. Fan, Z. Yu, X. Hu, T. James, X. He, T. Tang, Preferential Colonization of osteoblasts over Co-cultured Bacteria on a Bifunctional biomaterial surface, Front. Microbiol. 9 (2018), https://doi.org/10.3389/fmicb.2018.02219.

[61] P. Carmeliet, R. Jain, Angiogenesis in Cancer and other diseases, Nature 407 (2000) 249–257, https://doi.org/10.1038/35025220.

[62] A. Kusumbe, S. Ramasamy, R. Adams, Coupling of angiogenesis and osteogenesis by a specific vessel Subtype in bone, Nature 507 (7492) (2014) 323–328, https://doi.org/10.1038/nature13145.

[63] J. An, H. Yang, Q. Zhang, C. Liu, J. Zhao, L. Zhang, B. Chen, Natural products for treatment of Osteoporosis: the effects and mechanisms on promoting osteoblast-mediated bone formation, Life Sci. 147 (2016) 46–58, https://doi.org/10.1016/j.lfs.2016.01.024.

[64] K. Nakashima, X. Zhou, G. Kunkel, Z. Zhang, J. Deng, R. Behringer, B. Crombrugghe, The novel zinc Finger-containing Transcription factor Osterix is required for osteoblast differentiation and bone formation, Cell 108 (2002) 12, https://doi.org/10.1016/S0092-8674(01)00622-5.

[65] J. Li, F. Han, J. Ma, H. Wang, J. Pan, G. Yang, H. Zhao, J. Zhao, J. Liu, Z. Liu, B. Li, Targeting Endogenous hydrogen peroxide at bone defects promotes bone repair, Adv. Funct. Mater. 32 (10) (2021), https://doi.org/10.1002/adfm.202111208.

[66] S. Maeno, Y. Niki, H. Matsumoto, H. Morioka, T. Yatabe, A. Funayama, Y. Toyama, T. Taguchi, J. Tanaka, The effect of calcium ion concentration on osteoblast viability, proliferation and differentiation in Monolayer and 3D culture, Biomaterials 26 (23) (2005) 4847–4855, https://doi.org/10.1016/j.biomaterials.2005.01.006.

[67] S. Nakamura, T. Matsumoto, J. Sasaki, H. Egusa, K. Lee, T. Nakano, T. Sohmura, A. Nakahira, Effect of calcium ion concentrations on osteogenic differentiation and Hematopoietic stem cell Niche-related protein expression in osteoblasts, Tissue Eng. Part A 16 (8) (2010) 2467–2473, https://doi.org/10.1089/ten.tea.2009.0337.

[68] J. Rouwkema, A. Khademhosseini, Vascularization and angiogenesis in tissue engineering: beyond creating static networks, Trends Biotechnol. 34 (9) (2016) 733–745, https://doi.org/10.1016/j.tibtech.2016.03.002.

[69] C. Vitale-Brovarone, F. Baino, M. Miola, R. Mortera, B. Onida, E. Verné, Glass–ceramic scaffolds containing Silica Mesophases for bone grafting and drug delivery, J. Mater. Sci. Mater. Med. 20 (3) (2008) 809–820, https://doi.org/10.1007/s10856-008-3635-7.

[70] S. Suvarnapathaki, M. Nguyen, A. Goulopoulos, D. Lantigua, G. Camci-Unal, Engineering calcium peroxide based oxygen generating scaffolds for tissue survival, Biomater. Sci. 9 (7) (2021) 2519–2532, https://doi.org/10.1039/d0bm02048f.

[71] J. Zhao, C. Zhou, Y. Xiao, K. Zhang, Q. Zhang, L. Xia, B. Jiang, C. Jiang, W. Ming, H. Zhang, H. Long, W. Liang, Oxygen generating biomaterials at the Forefront of regenerative Medicine: Advances in bone regeneration, Front. Bioeng. Biotechnol. 12 (2024), https://doi.org/10.3389/fbioe.2024.1292171.

[72] C. Lu, N. Saless, X. Wang, A. Sinha, S. Decker, G. Kazakia, H. Hou, B. Williams, H. Swartz, T. Hunt, T. Miclau, R. Marcucio, The role of oxygen during fracture healing, Bone 52 (1) (2013) 220–229, https://doi.org/10.1016/j.bone.2012.09.037.

[73] Q. Liu, Y. Zhuang, N. Ouyang, H. Yu, Cytochalasin D promotes osteogenic differentiation of MC3T3-E1 cells via p38-MAPK signaling pathway, Curr. Mol. Med. 20 (1) (2019) 79–88, https://doi.org/10.2174/1566524019666191007104816.

[74] M. Wu, G. Chen, Y. Li, TGF-B and BMP signaling in osteoblast, Skeletal development, and bone formation, Homeostasis and disease, Bone Res. 4 (1) (2016), https://doi.org/10.1038/boneres.2016.9.

[75] K. Kim, J. Kim, I. Kim, S. Seong, N. Kim, Rev-erbα Negatively regulates Osteoclast and osteoblast differentiation through p38 MAPK signaling pathway, Mol. Cells 43 (1) (2020) 34–47, https://doi.org/10.14348/molcells.2019.0232.

[76] J. Jann, S. Gascon, S. Roux, N. Faucheux, TGF-B signaling on Balancing osteoblast, Osteoclast and Chondrocyte, Int. J. Mol. Sci. 21 (20) (2020) 7597, https://doi.org/10.16476/j.pibb.2021.0060.

[77] Y. Lu, Q. Zhao, Y. Liu, L. Zhang, D. Li, Z. Zhu, X. Gan, H. Yu, Vibration loading promotes osteogenic differentiation of bone Marrow-derived Mesenchymal stem cells via p38 MAPK signaling pathway, J. Biomech. 71 (2018) 67–75, https://doi.org/10.1016/j.jbiomech.2018.01.039.

[78] H. Kim, N. Oh, M. Kwon, O. Kwon, S. Ku, J. Seo, S. Roh, Exopolysaccharide of Enterococcus Faecium L15 promotes the osteogenic differentiation of Human Dental Pulp stem cells via p38 MAPK pathway, Stem Cell Res. Ther. 13 (1) (2022), https://doi.org/10.1186/s13287-022-03151-0.

[79] Ł.A. Poniatowski, P. Wojdasiewicz, R. Gasik, D. Szukiewicz, Transforming growth factor Beta Family: Insight into the role of growth factors in regulation of fracture healing Biology and potential clinical applications, Mediat. Inflamm. 2015 (2015) 1–17, https://doi.org/10.1155/2015/137823.

[80] W. Huang, S. Yang, J. Shao, Y. Li, Signaling and Transcriptional regulation in osteoblast Commitment and differentiation, Front. Biosci. 12 (2007) 3068–3092, https://doi.org/10.2741/2296.

[81] C. Loveridge, J. Hesketh, S. Jakowlew, C. Whitehead, B. Thorp, The control of Chondrocyte differentiation during Endochondral bone growth *in vivo*: Changes in TGF-β and the Proto-oncogene c-myc, J. Cell Sci. 105 (4) (1993) 949–956, https://doi.org/10.1242/jcs.105.4.949.

[82] B. Selvarajah, I. Azuelos, M. Platé, D. Guillotin, E. Forty, G. Contento, H. Woodcock, M. Redding, A. Taylor, G. Brunori, P. Durrenberger, R. Ronzoni, A. Blanchard, P. Mercer, D. Anastasiou, R. Chambers, mTORC1 Amplifies the ATF4-dependent De Novo serine-glycine pathway to supply Glycine during TGF-β1–induced collagen Biosynthesis, Sci. Signal. 12 (582) (2019), https://doi.org/10.1126/scisignal.aav3048.

[83] F. Yang, D.W. Richardson, Y. Jiang, Comparative analysis of Tenogenic gene expression in Tenocyte-derived induced Pluripotent stem cells and bone Marrow-derived Mesenchymal stem cells in response to Biochemical and Biomechanical Stimuli, Stem Cell. Int. 2021 (2021) 1–18, https://doi.org/10.1155/2021/8835576.

[84] O. Ishibashi, T. Inui, Identification of Endoglin-dependent BMP-2-induced genes in the Murine Periodontal Ligament cell line PDL-L2, J. Mol. Signal. 9 (2014), 0.1186/1750-2187-9-5.

[85] M. Sinkala, P. Nkhoma, N. Mulder, D. Martin, Integrated molecular Characterisation of the MAPK pathways in Human Cancers reveals Pharmacologically Vulnerable Mutations and gene Dependencies, Commun. Biol. 4 (1) (2021), https://doi.org/10.1038/s42003-020-01552-6.